

ALMA CO Observations of the Mixed-Morphology Supernova Remnant W49B: Efficient Production of Recombining Plasma and Hadronic Gamma-rays via Shock–Cloud Interactions

H. SANO ¹, S. YOSHIKE ², Y. YAMANE ², K. HAYASHI ³, R. ENOKIYA ⁴, K. TOKUDA ^{1,5}, K. TACHIHARA ²,
G. ROWELL ⁶, M. D. FILIPOVIĆ ⁷ AND Y. FUKUI ²

¹National Astronomical Observatory of Japan, Mitaka, Tokyo 181-8588, Japan; hidetoshi.sano@nao.ac.jp

²Department of Physics, Nagoya University, Furo-cho, Chikusa-ku, Nagoya 464-8601, Japan

³Institute of Space and Astronautical Science (ISAS), Japan Aerospace Exploration Agency (JAXA), 3-1-1, Yoshinodai, Chuo-ku, Sagami-hara, Kanagawa 252-5210, Japan

⁴Department of Physics, Institute of Science and Technology, Keio University, 3-14-1 Hiyoshi, Kohoku-ku, Yokohama, Kanagawa 223-8522, Japan

⁵Department of Physical Science, Graduate School of Science, Osaka Prefecture University, 1-1 Gakuen-cho, Naka-ku, Sakai 599-8531, Japan

⁶School of Physical Sciences, The University of Adelaide, North Terrace, Adelaide, SA 5005, Australia

⁷Western Sydney University, Locked Bag 1797, Penrith South DC, NSW 1797, Australia

ABSTRACT

We carried out new CO($J = 2-1$) observations toward the mixed-morphology supernova remnant (SNR) W49B with the Atacama Large Millimeter/submillimeter Array (ALMA). We found that CO clouds at ~ 10 km s⁻¹ show a good spatial correspondence with synchrotron radio continuum as well as an X-ray deformed shell. The bulk mass of molecular clouds accounts for the western part of the shell, not for the eastern shell where near-infrared H₂ emission is detected. The molecular clouds at ~ 10 km s⁻¹ show higher kinetic temperature of $\sim 20-60$ K, suggesting that modest shock-heating occurred. The expanding motion of the clouds with $\Delta V \sim 6$ km s⁻¹ was formed by strong winds from the progenitor system. We argue that the barrel-like structure of Fe rich ejecta was possibly formed not only by an asymmetric explosion, but also by interactions with dense molecular clouds. We also found a negative correlation between the CO intensity and the electron temperature of recombining plasma, implying that the origin of the high-temperature recombining plasma in W49B can be understood as the thermal conduction model. The total energy of accelerated cosmic-ray protons W_p is estimated to be $\sim 2 \times 10^{49}$ erg by adopting an averaged gas density of $\sim 650 \pm 200$ cm⁻³. The SNR age– W_p diagram indicates that W49B shows one of the highest in-situ values of W_p in the gamma-ray bright SNRs.

Keywords: Supernova remnants (1667); Interstellar medium (847); Cosmic ray sources (328); Gamma-ray sources (633); X-ray sources (1822)

1. INTRODUCTION

Mixed-morphology supernova remnants (SNRs) are characterized a center-filled thermal X-ray morphology with a synchrotron radio shell, accounting for more than 25% of Galactic SNRs (Rho & Petre 1998). Most of the mixed-morphology SNRs are interacting with the dense interstellar medium (ISM) evidenced by radio-line emission such as CO, H I, and/or 1720 MHz OH masers (e.g., Seta et al. 1998; Yusef-Zadeh et al. 2003; Kuriki et al. 2018). In addition, some of them are associated with GeV/TeV gamma-ray sources, which likely arise from interactions between accelerated cosmic-ray (CR) protons and dense clouds in the vicinity of the SNRs (e.g., Aharonian et al. 2008; Bamba et al. 2016). Moreover, shock-propagation into the clumpy ISM and/or dense circumstellar matter (CSM) have a potential to explain their mixed-morphology and thermal X-ray radiation (e.g.,

Shimizu et al. 2012; Slavin et al. 2017; Zhang et al. 2019). Therefore, the shock-interacting ISM plays an important role in understanding their morphology, plasma conditions, and cosmic-ray acceleration (see also reviews by Vink 2012; Yamaguchi 2020; Sano & Fukui 2021). To unveil the physical processes and high-energy phenomena in the mixed-morphology SNRs, detailed comparative studies among the radio-line emission, X-rays, and gamma-rays are needed.

W49B (also known as G43.3–0.2) is a well-studied Galactic mixed-morphology SNR with the bright radio-continuum shell and thermal-dominated center-filled X-rays as shown in Figure 1. The SNR is thought to be lying on the far-side of the Galaxy from us (e.g., Lockhart & Goss 1978; Brogan & Troland 2001). The small apparent diameter of $\sim 3'-5'$ is consistent with the larger distance of $\sim 7.5-11.3$ kpc (Zhu et al. 2014; Ranasinghe & Leahy 2018; Lee et al. 2020) and its young age (5–

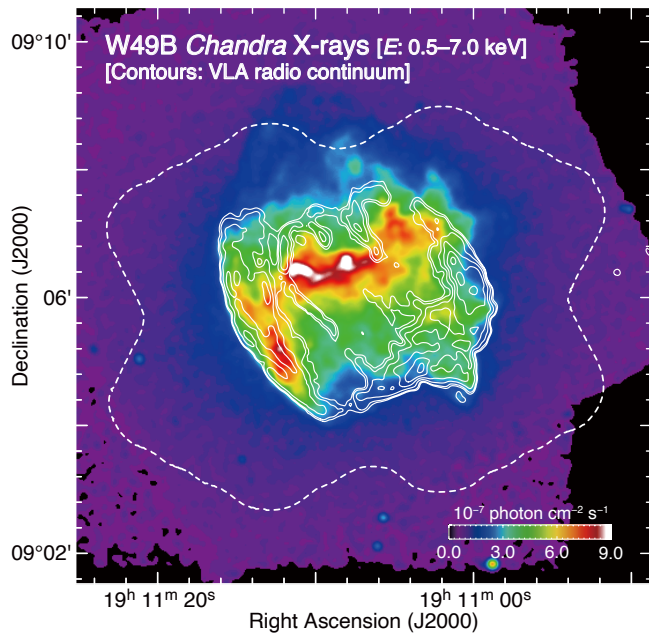


Figure 1. Intensity map of *Chandra* broad-band X-rays (E : 0.5–7.0 keV, e.g., Lopez et al. 2013b) superposed on the VLA radio continuum contours at 20 cm obtained from MAGPIS (Helfand et al. 2006). The contour levels are 5.0, 7.6, 15.4, 28.4, 46.6, and 70.0 mJy beam $^{-1}$. The region enclosed by dashed rectangle corresponds to the observed region with ALMA ACA.

6 kyr, Zhou & Vink 2018). W49B is also thought to be an efficient accelerator of CR protons owing to its bright GeV/TeV gamma-rays with the pion-decay bump (H. E. S. S. Collaboration et al. 2018). The total energy of CR protons was derived to be $\sim 10^{49}$ – 10^{51} erg, assuming the targeted gas density of 10–1000 cm $^{-3}$ (Abdo et al. 2010).

The X-ray radiation of W49B is characterized by three properties: the most luminous in Fe K-shell line emission (Yamaguchi et al. 2014), non-thermal Bremsstrahlung (Tanaka et al. 2018), and recombining (overionized) plasma where the ionization temperature goes even higher than the electron temperature (Ozawa et al. 2009; Miceli et al. 2010; Lopez et al. 2013a; Zhou & Vink 2018; Yamaguchi et al. 2018; Sun & Chen 2020; Holland-Ashford et al. 2020; Siegel et al. 2020). The elongated structure of Fe-rich ejecta is believed to be related to a bipolar/jet-driven Type Ib/Ic explosion and/or interactions between the shock and a surrounding interstellar cloud (Keohane et al. 2007; Lopez et al. 2013b; Bear & Soker 2017). On the other hand, recent X-ray studies on metal abundances favor Type Ia models (Zhou & Vink 2018; Siegel et al. 2020). Additionally, Sun & Chen (2020) conclude that the SN type is unclear, with neither core-collapse or Ia models perfectly reproduc-

ing their best-fit abundances. The origin of recombining plasma—thermal conduction with cold-dense clouds and/or adiabatic cooling—is still being debated (e.g., Yamaguchi et al. 2018; Sun & Chen 2020; Holland-Ashford et al. 2020). If we detect decreasing the electron temperature toward the shocked clouds, we can confirm the thermal conduction scenario as a formation mechanism of the recombination plasma (e.g., Matsumura et al. 2017b; Okon et al. 2018, 2020).

Although W49B is thought to be interacting with interstellar clouds, it is a perplexing question which clouds are physically associated. Keohane et al. (2007) discovered 2.12 μ m shocked H $_2$ emission toward the eastern and southwestern shells by near-infrared photometric observations. The total mass of shocked H $_2$ is estimated to 14–550 M_{\odot} . Subsequent radio observations using CO line emission revealed three molecular clouds at velocities of ~ 10 , ~ 40 , and ~ 60 km s $^{-1}$, which are possibly associated with the SNR (e.g., Zhu et al. 2014; Kilpatrick et al. 2016; Lee et al. 2020). Zhu et al. (2014) argued that the molecular cloud at ~ 40 km s $^{-1}$ is interacting with W49B because of its wind-bubble like morphology. On the other hand, Kilpatrick et al. (2016) found a line-broadening of 12 CO profile in a molecular cloud at ~ 10 km s $^{-1}$ located toward the western shell of W49B, and hence the authors claimed that the cloud at 10 km s $^{-1}$ is interacting with the SNR. The velocity is roughly consistent with the H I absorption studies (Brogan & Troland 2001; Ranasinghe & Leahy 2018). Most recently, Lee et al. (2020) performed near-infrared spectroscopy of shocked H $_2$ emission toward four strips on W49B. The authors found that a central velocity of shocked H $_2$ is ~ 64 km s $^{-1}$ and then concluded that the molecular cloud at ~ 60 km s $^{-1}$ located toward the center and the southwest shell of W49B is likely associated with the SNR. In either case, detailed spatial and kinematic studies as well as deriving cloud properties (e.g., mass, density, kinetic temperature) have not been performed due to the modest sensitivity and angular resolution of CO datasets up to $\sim 20''$, corresponding to a spatial resolution of ~ 1 pc at the distance of 10 kpc.

In the present paper, we report on results of new millimeter wavelength observations using CO($J = 2-1$) line emission with the Atacama Compact Array (ACA, also known as Morita Array) which is a part of the Atacama Large Millimeter/submillimeter Array (ALMA). The unprecedented sensitivity and high-angular resolution of $\sim 7''$ (~ 0.3 pc at the distance of 10 kpc) of the ALMA CO data enable us to identify the interacting molecular cloud and its physical relation to the high-energy phenomena in W49B. Section 2 describes the observational datasets and reductions. Section 3 comprises five subsections: Sections 3.1–3.3 present overview distributions of X-ray, radio continuum, and CO; Section 3.4–3.5 show physical conditions of molecular clouds. Discussion and conclusions are given in Sections 4 and 5, respectively.

2. OBSERVATIONS AND DATA REDUCTIONS

2.1. CO

Observations of $^{12}\text{CO}(J = 2-1)$ and $^{13}\text{CO}(J = 2-1)$ line emission were conducted using ALMA ACA Band 6 (211–275 GHz) as a Cycle 6 project (proposal no. 2018.1.01780.S). We used the mosaic observation mode with 10–12 antennas of 7-m array and four antennas of 12-m total power (TP) array. The observed areas were $5'.1 \times 2'.7$ rectangular regions centered at $(\alpha_{\text{J2000}}, \delta_{\text{J2000}}) = (19^{\text{h}}11^{\text{m}}09^{\text{s}}00, +9^{\circ}06'24''.8)$ and $(19^{\text{h}}11^{\text{m}}07^{\text{s}}44, +9^{\circ}05'56''.2)$. The actual observed area is shown in Figure 1. The combined baseline length of 7-m array data is from 8.85 to 48.95 m, corresponding to $u-v$ distances from 6.8 to $37.6 k\lambda$ at 230.538 GHz. Two quasars, J1924–2914 and J1751+0939, were observed as bandpass and flux calibrators. We also observed four quasars, J1907+0127, J1922+1530, J1938+0448, and J1851+0035, as phase calibrators. We performed data reduction using the Common Astronomy Software Application (CASA, McMullin et al. 2007) package version 5.5.0. We utilized “*tclean*” task with multi-scale deconvolver and natural weighting. The emission mask was also selected using the auto-multithresh procedure (Kepley et al. 2020). We combined the cleaned 7-m array data and the calibrated TP array data using “*feather*” task to recover the missing flux and diffuse emission. The beam size of feathered data is $8''.23 \times 4''.77$ with a position angle of -75.31° for the $^{12}\text{CO}(J = 2-1)$ data, and $8''.28 \times 5''.04$ with a position angle of -79.37° for the $^{13}\text{CO}(J = 2-1)$ data. The typical noise fluctuations are ~ 0.065 K for the $^{12}\text{CO}(J = 2-1)$ data and ~ 0.055 K for the $^{13}\text{CO}(J = 2-1)$ data at the velocity resolution of 0.4 km s^{-1} .

We also used archival datasets of $^{12}\text{CO}(J = 1-0)$ and $^{12}\text{CO}(J = 3-2)$ line emission for estimating physical properties of molecular clouds. The $^{12}\text{CO}(J = 1-0)$ data are from the FOREST Unbiased Galactic Plane Imaging survey with the Nobeyama 45 m telescope (FUGIN, Umemoto et al. 2017), and the $^{12}\text{CO}(J = 3-2)$ data are from the CO High-Resolution Survey (COHRS, Dempsey et al. 2013) obtained with the James Clerk Maxwell Telescope (JCMT). The angular resolution is $\sim 20''$ for the $^{12}\text{CO}(J = 1-0)$ data and $\sim 16''.6$ for the $^{12}\text{CO}(J = 3-2)$ data. The velocity resolutions of $^{12}\text{CO}(J = 1-0)$ and $^{12}\text{CO}(J = 3-2)$ data are 1.3 and 1.0 km s^{-1} , respectively. To improve the signal-to-noise ratio of the $^{12}\text{CO}(J = 3-2)$ data, we combined four spatial pixels and a rebinned pixel size is to be $12''$. The typical noise fluctuations are ~ 1.4 K for the $^{12}\text{CO}(J = 1-0)$ data and ~ 0.18 K for the $^{12}\text{CO}(J = 3-2)$ data at each velocity resolution.

2.2. Radio Continuum

The radio continuum data at 20 cm wavelength are from the Multi-Array Galactic Plane Imaging Survey (MAGPIS, Helfand et al. 2006) obtained with the Very

Large Array (VLA) and the Effelsberg 100-m telescope. The angular resolution is $\sim 6''$, which is compatible for the ALMA ACA resolution. The typical noise fluctuations are $\sim 1-2 \text{ mJy}$.

2.3. X-rays

We utilized archival X-ray data obtained by *Chandra* (observation IDs are 117, 13440, and 13441), which have been published in numerous papers (e.g., Kawasaki et al. 2005; Lopez et al. 2009a,b, 2011, 2013a,b; Yang et al. 2009; Koo et al. 2016; Zhou & Vink 2018). The X-ray datasets were taken with the Advanced CCD Imaging Spectrometer S-array (ACIS-S3). We used *Chandra* Interactive Analysis of Observations (CIAO, Fruscione et al. 2006) software version 4.12 with CALDB 4.9.1 (Graessle et al. 2007) for data reduction and imaging. After reprocessing for all datasets using the “*chandra_repro*” procedure, we created an energy-filtered, exposure-corrected image using the “*fluximage*” procedure in the energy bands of 0.5–7.0 keV (broad-band, see Figure 1), 0.5–1.2 keV (soft-band), 1.2–2.0 keV (medium band), 2.0–7.0 keV (hard-band), and 4.2–5.5 keV (continuum band). Because the soft- and medium-band images are heavily affected by interstellar absorption (e.g., Zhou & Vink 2018), in this paper we focus on the X-ray images at energies greater than 2.0 keV. We also created an exposure-corrected, continuum-subtracted image of Fe He α line emission (6.4–6.9 keV) following the method presented by Lopez et al. (2013b). The typical angular resolution of *Chandra* images is $\sim 0''.5$.

3. RESULTS

3.1. Overview of X-ray, Radio Continuum, and CO Distributions

Figure 1 shows the *Chandra* broad-band X-ray image of W49B superposed on the VLA radio continuum contours at 20 cm wavelength. As presented in previous studies, a barrel-shaped radio-continuum shell with several co-axis filaments and the center-filled X-rays are seen (e.g., Keohane et al. 2007; Lopez et al. 2009a, 2011). The X-ray elongated feature brighter than $\sim 5 \times 10^{-7} \text{ photon cm}^{-2} \text{ s}^{-1}$ is roughly consistent with the spatial distribution of Fe He α emission (see Figure 3 in Lopez et al. 2013b). We note that overall distributions of X-rays and radio continuum are quite different between the northeastern and southwestern halves: the shell boundary of the northeastern half roughly coincides with each other, whereas the southwestern shell of X-rays is significantly deformed compared to that of radio continuum. In particular, the X-rays are dim around positions at $(\alpha_{\text{J2000}}, \delta_{\text{J2000}}) \sim (19^{\text{h}}11^{\text{m}}00^{\text{s}}0, +09^{\circ}06'00'')$, $(19^{\text{h}}11^{\text{m}}03^{\text{s}}0, +09^{\circ}05'00'')$, and $(19^{\text{h}}11^{\text{m}}08^{\text{s}}0, +09^{\circ}06'06'')$: the first two correspond to the bright peaks of radio-continuum and the other is partially surrounded by radio filaments. This trend is also seen in the 4.2–5.5 keV band image which is

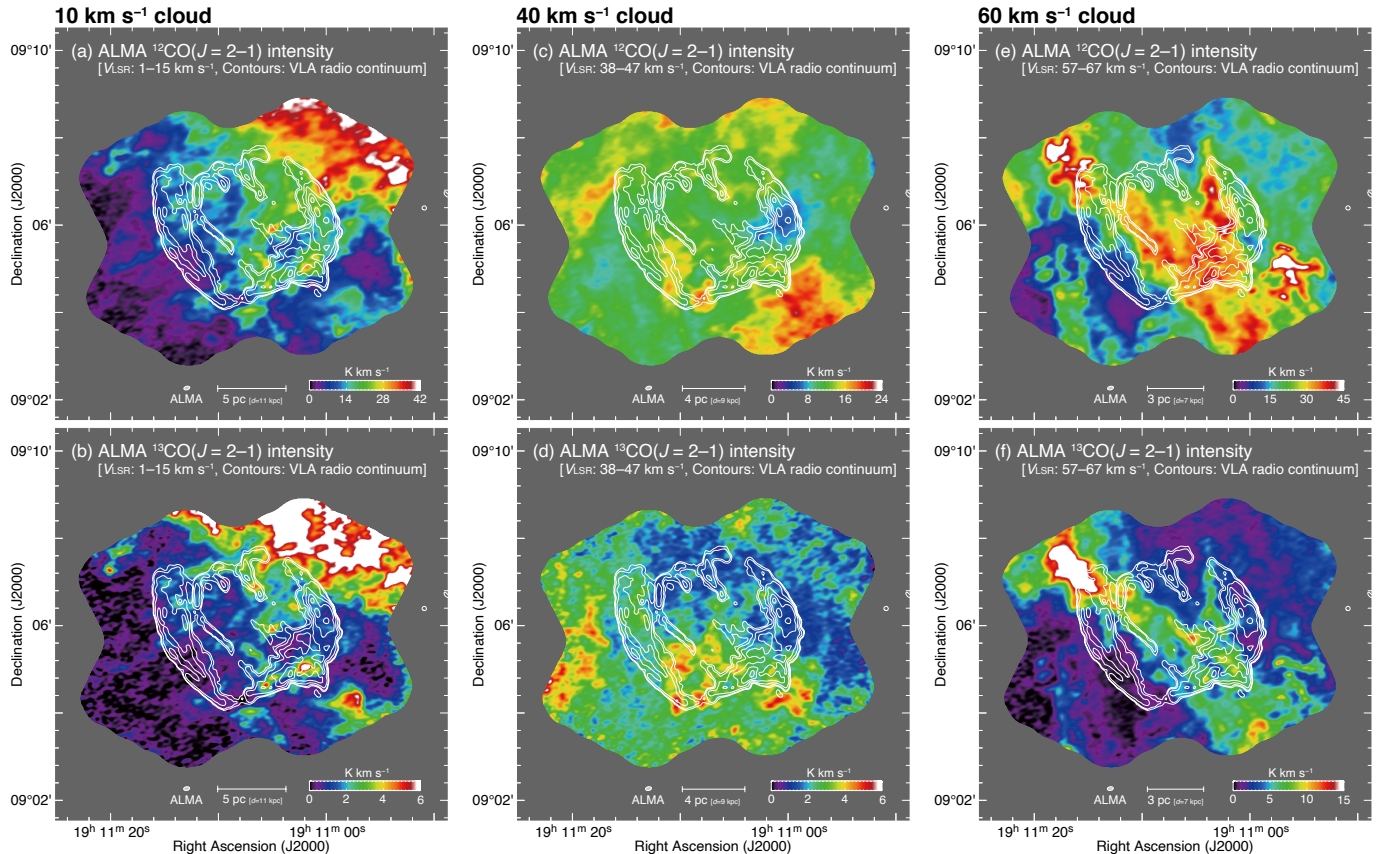


Figure 2. Integrated intensity maps of ALMA ACA $^{12}\text{CO}(J = 2-1)$ (*upper panels*) and $^{13}\text{CO}(J = 2-1)$ (*lower panels*) for (a, b) the 10 km s^{-1} cloud, (c, d) the 40 km s^{-1} cloud, and (e, f) the 60 km s^{-1} cloud. The integration velocity range is from 1 to 15 km s^{-1} for the 10 km s^{-1} cloud; from 38 to 47 km s^{-1} for the 40 km s^{-1} cloud; and is from 57 to 67 km s^{-1} for the 60 km s^{-1} cloud. Superposed contours are the same as shown in Figure 1.

mostly free from the interstellar absorption as well as line-emission.

Figure 2 shows integrated intensity maps of $^{12}\text{CO}(J = 2-1)$ and $^{13}\text{CO}(J = 2-1)$ for three velocity ranges of $1-15 \text{ km s}^{-1}$ (hereafter “ 10 km s^{-1} cloud”), $38-47 \text{ km s}^{-1}$ (hereafter “ 40 km s^{-1} cloud”), and $57-67 \text{ km s}^{-1}$ (hereafter “ 60 km s^{-1} cloud”) as previously mentioned in several papers (e.g., Zhu et al. 2014; Kilpatrick et al. 2016; Lee et al. 2020). The kinematic distance of molecular cloud is $\sim 11 \text{ kpc}$ for the 10 km s^{-1} cloud; $\sim 9 \text{ kpc}$ for the 40 km s^{-1} cloud¹; and $\sim 7 \text{ kpc}$ for the 60 km s^{-1} cloud (Sofue et al. 2020). Note that there are no other CO clouds within the velocity range from -15.0 to

¹ Although Zhu et al. (2014) suggested the distance of 40 km s^{-1} cloud to be $\sim 10 \text{ kpc}$ using a Galactic rotation curve model with $R_0 = 8.5 \text{ kpc}$ and $\Theta_0 = 220 \text{ km s}^{-1}$ (Kerr & Lynden-Bell 1986), we adopt its distance to be $\sim 9 \text{ kpc}$ using the latest Galactic parameters of $R_0 = 7.92 \text{ kpc}$ and $\Theta_0 = 227 \text{ km s}^{-1}$ (VERA Collaboration et al. 2020). Here R_0 is the distance from the Sun to the Galactic center and Θ_0 is the rotation velocity of the local standard of rest. We use the latter values throughout the paper.

92.6 km s^{-1} , and hence we focus on the three molecular clouds in the present paper.

In the 10 km s^{-1} cloud (Figures 2a and 2b), there is an intensity gradient increasing from southeast to northwest. The radio continuum shows fairly good spatial correspondence with molecular clouds in the northern inward protrusion and along the north, northwest, and southwest rims. On the other hand, both the ^{12}CO and ^{13}CO emission lines are faint in the southeastern shell where shocked H_2 emission is strongly detected (e.g., Keohane et al. 2007). Dense clouds traced by ^{13}CO emission are located not only outside the shell boundary, but also inside the radio continuum shell.

In the 40 km s^{-1} cloud (Figures 2c and 2d), the ^{12}CO emission has a relatively uniform distribution rather than that of the 10 km s^{-1} cloud, but the ^{13}CO emission shows an intensity gradient increasing from northwest to southeast. We note that the radio brightest shell in west shows lack of both the ^{12}CO and ^{13}CO emission lines. The bright ^{12}CO emission and ^{13}CO clumps are located both toward the southwest of the SNR as well as inside the southeastern shell. The southwestern CO clumps seem to be along the sharp edge of radio shell, whereas

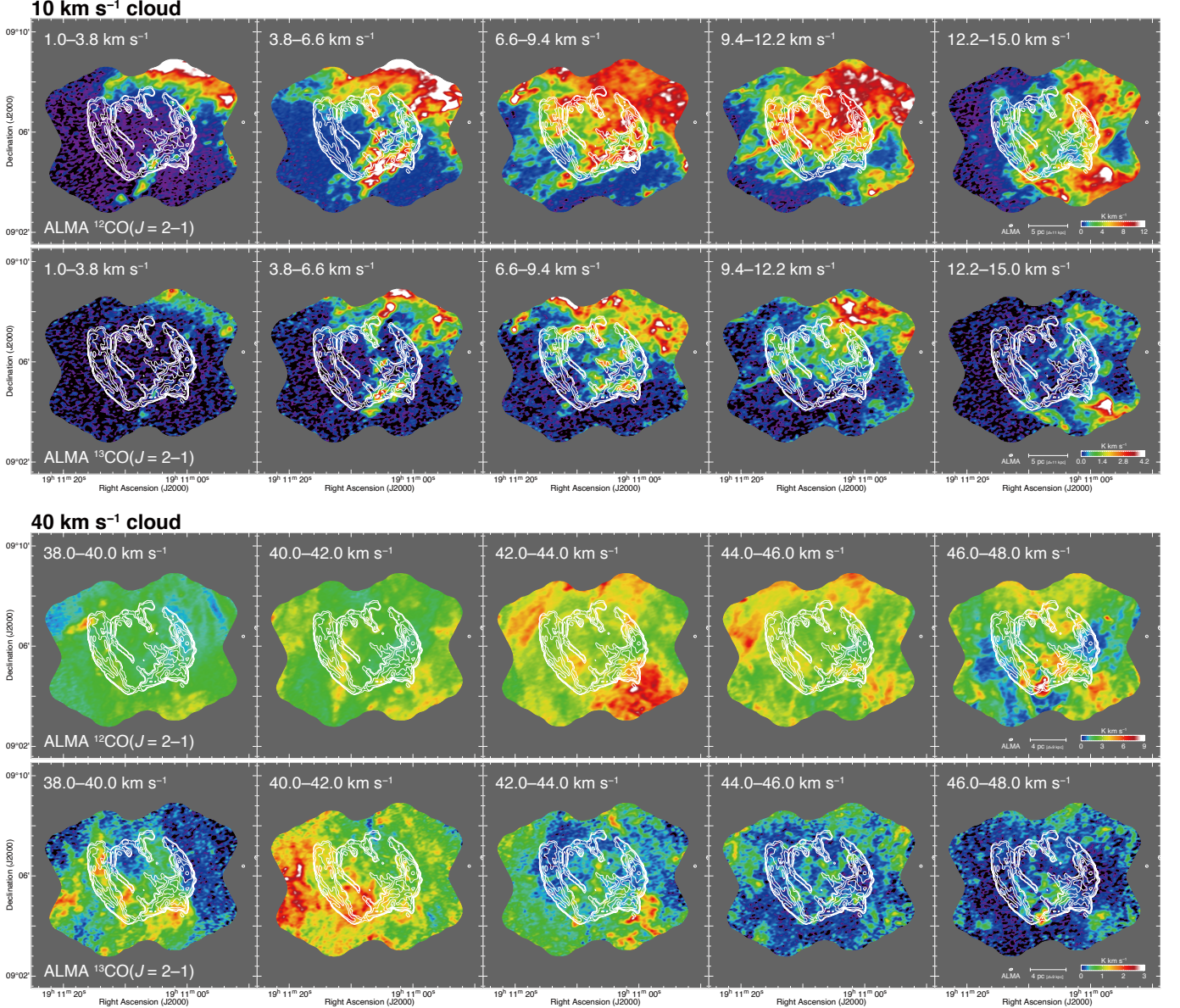


Figure 3. Velocity channel maps of ALMA ACA $^{12}\text{CO}(J = 2-1)$ (*upper panels*) and $^{13}\text{CO}(J = 2-1)$ (*lower panels*) for each cloud. Each panel shows CO integrated intensity distribution integrated over the velocity range from 1 to 15 km s⁻¹ every 2.8 km s⁻¹ for the 10 km s⁻¹ cloud; from 38 to 48 km s⁻¹ every 2 km s⁻¹ for the 40 km s⁻¹ cloud; and 57 to 67 km s⁻¹ every 2 km s⁻¹ for the 60 km s⁻¹ cloud. Superposed contours are the same as shown in Figure 1.

the CO clumps inside the SNR show no significant spatial correlations with the radio shell morphology. At this spatial coverage, we could not find the bubble-like CO structure toward W49B as mentioned by [Zhu et al. \(2014\)](#).

In the 60 km s⁻¹ cloud (Figures 2e and 2f), there are dense clouds across the SNR from northeast to southwest with two bright CO peaks at $(\alpha_{J2000}, \delta_{J2000}) \sim (19^{\text{h}}11^{\text{m}}17^{\text{s}}.0, +09^{\circ}07'30'')$ and $(19^{\text{h}}10^{\text{m}}57^{\text{s}}.5, +09^{\circ}05'07'')$. The former contains two H II regions cataloged by [Urquhart et al. \(2009\)](#), whereas the latter does not have any cataloged objects. The diffuse CO emission

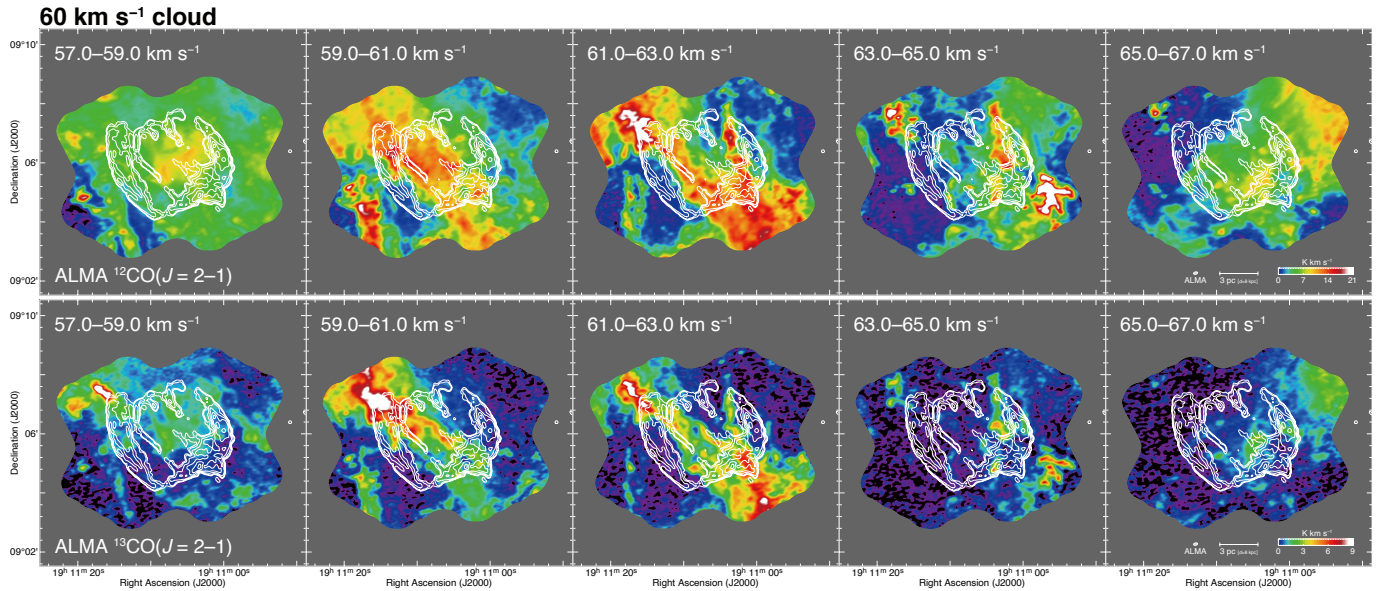
inside the SNR appears to be spatially anti-correlated with the radio continuum contours.

To derive masses of three molecular clouds, we used the following equations:

$$M = m_{\text{H}}\mu\Omega D^2 \sum_i N_i(\text{H}_2), \quad (1)$$

$$N(\text{H}_2) = X \cdot W(\text{CO}), \quad (2)$$

where m_{H} is the mass of hydrogen, $\mu = 2.8$ is the mean molecular weight, Ω is the solid angle of each pixel, D is the distance to W49B, $N_i(\text{H}_2)$ is the column density of molecular hydrogen for each pixel, X is CO-to-

Figure 3. *Continued.*

H_2 conversion factor of $2 \times 10^{20} \text{ cm}^{-2} (\text{K km s}^{-1})^{-1}$ (Bertsch et al. 1993), and $W(\text{CO})$ is the velocity-integrated intensity of $^{12}\text{CO}(J = 1-0)$ emission line obtained from the FUGIN data (Umemoto et al. 2017). We estimated the mass of molecular cloud inside the radio shell to be $\sim 4.1 \times 10^4 M_\odot$ for the 60 km s^{-1} cloud and $\sim 2.7 \times 10^4 M_\odot$ for the other two clouds, where we adopted the shell radius of 2.5 centered at $(\alpha_{\text{J2000}}, \delta_{\text{J2000}}) = (19^{\text{h}}11^{\text{m}}07^{\text{s}}.34, +09^{\circ}06'01''.1)$. These values are roughly consistent with previously derived cloud masses using the $^{13}\text{CO}(J = 1-0)$ emission and the ^{13}CO -to- H_2 conversion factor (H. E. S. S. Collaboration et al. 2018).

3.2. Detailed Spatial Comparison with the Radio Continuum Shell

Figure 3 shows velocity channel maps for each molecular cloud superposed on the radio continuum contours. We find that dense ^{13}CO clumps at a velocity range from 3.8 to 9.4 km s^{-1} are nicely along not only with the northern and southern shell, but also with radio filaments inside the SNR at positions of $(\alpha_{\text{J2000}}, \delta_{\text{J2000}}) \sim (19^{\text{h}}11^{\text{m}}06^{\text{s}}.4, +09^{\circ}07'03'')$ and $(19^{\text{h}}11^{\text{m}}05^{\text{s}}.5, +09^{\circ}05'56'')$. We also find that both the ^{12}CO and ^{13}CO clouds at the velocity range of 9.4 – 12.2 km s^{-1} show global anti-correlation with the radio shell. In addition, ^{12}CO emission at the velocity range of 12.2 – 15.0 km s^{-1} shows a good spatial correspondence with the western shell especially for the sharp edge of the southwestern rim. This velocity range is consistent with that inferred from Kilpatrick et al. (2016). The southwestern CO clumps at 42.0 – 44.0 km s^{-1} seem to be along the sharp edge of radio shell especially prominent in the ^{13}CO line emission. Moreover, the ^{13}CO clouds at 38.0 – 40.0 km s^{-1} shows the good spatial correspondence with the southeastern half of the radio continuum shell. Fur-

thermore, the 63 – 65 km s^{-1} ^{12}CO map shows a lack of CO emission along the eastern shell and shows bright CO emission in the gaps between the western and northern radio contours. Although the other CO clouds also appear to be overlapped with the radio continuum shell and filaments, their spatial correspondence is not clear.

3.3. Position–Velocity Diagrams

Figure 4 shows position–velocity diagrams for the three molecular clouds. The velocity distributions of ^{12}CO and ^{13}CO emission are similar to each other except for a velocity at $\sim 40 \text{ km s}^{-1}$, suggesting that the ^{12}CO emission at $\sim 40 \text{ km s}^{-1}$ is subject to self-absorption due to optically thick component. In fact, the ^{12}CO emission at $\sim 40 \text{ km s}^{-1}$ shows dip-like feature, whereas the ^{13}CO spectrum at the same velocity has strong line emission. We also find incomplete and complete cavity-like structures in the 10 and 40 km s^{-1} clouds, respectively (see dashed curves in Figures 4a–4d). The incomplete cavity (or arc-like distribution) in the 10 km s^{-1} cloud lies from 5 km s^{-1} to 11 km s^{-1} with a velocity dispersion of a few km s^{-1} . On the other hand, the complete cavity in the 40 km s^{-1} cloud is clearly seen especially for ^{12}CO emission, whose velocity range is from 41 km s^{-1} to 47 km s^{-1} . Note that spatial extents of these cavities are roughly consistent with the diameter of the radio continuum shell. By contrast, there is no clear evidence for such cavity-like structure in the position–velocity diagram of the 60 km s^{-1} cloud (see Figures 4e and 4f).

3.4. Intensity Ratio Maps

Figure 5 shows intensity ratio maps of $^{12}\text{CO}(J = 3-2) / ^{13}\text{CO}(J = 2-1)$ (hereafter $R_{12\text{CO}32/13\text{CO}21}$) toward the three molecular clouds. A higher value of $R_{12\text{CO}32/13\text{CO}21}$ tends to be observed in diffuse warm

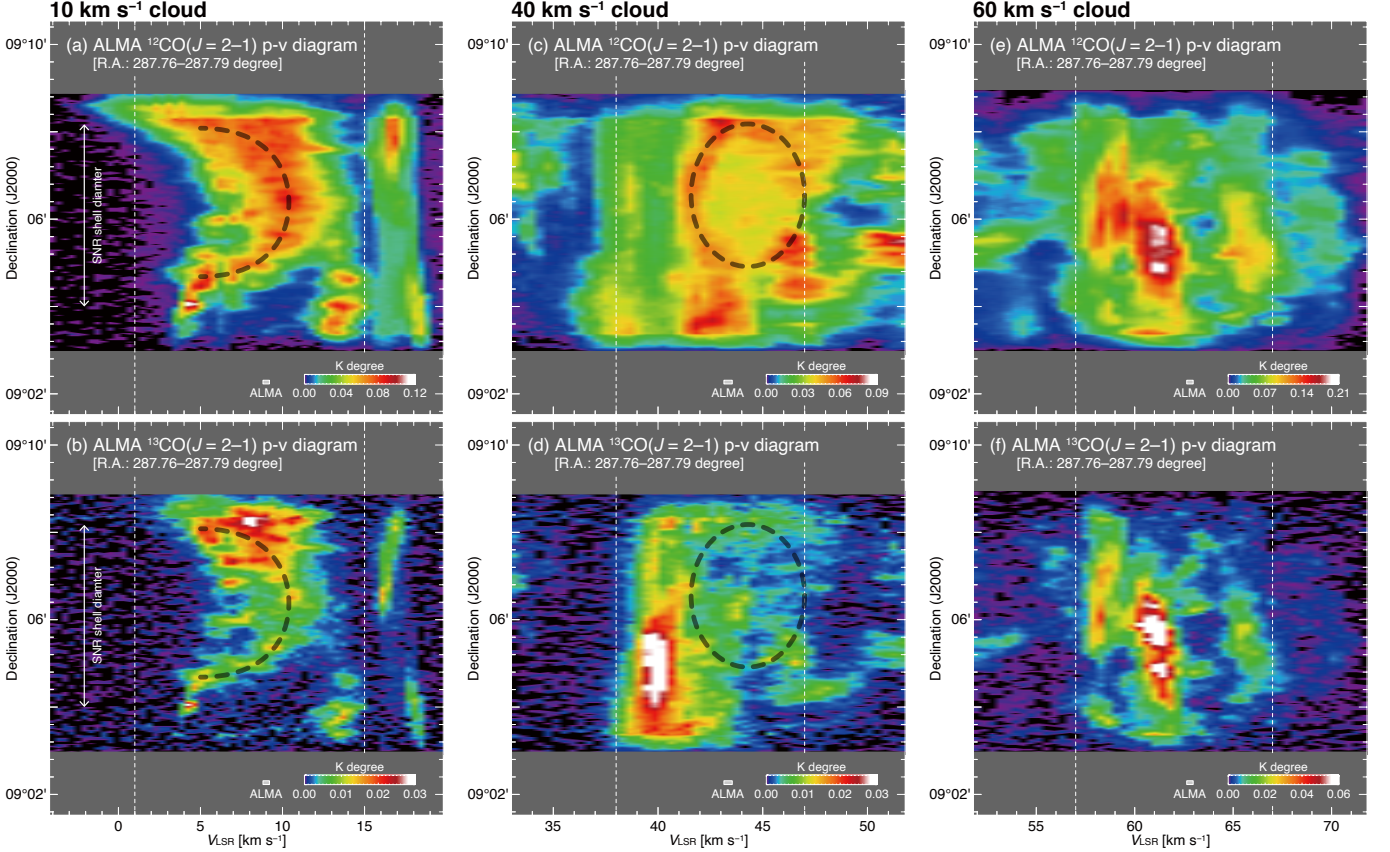


Figure 4. Position-velocity diagram of ALMA ACA $^{12}\text{CO}(J = 2-1)$ (*upper panels*) and $^{13}\text{CO}(J = 2-1)$ (*lower panels*) for (a, b) the 10 km s^{-1} cloud, (c, d) the 40 km s^{-1} cloud, and (e, f) the 60 km s^{-1} cloud. The integration range of Right Ascension is from $283^{\circ}.76$ to $287^{\circ}.79$. Dashed curves and circles delineate expanding gas motion (see the text). Vertical dashed lines indicate integration velocity ranges for each cloud.

gas thermalized by supernova shocks and/or stellar radiation assuming that the abundance ratio of $^{12}\text{CO}/^{13}\text{CO}$ is constant within a molecular cloud complex (cf. Biegging & Peters 2011; Dell’Ova et al. 2020). We find that high-intensity ratios of $R_{12\text{CO}32/13\text{CO}21} \sim 10$ are distributed toward the shell of W49B in the 10 km s^{-1} cloud. The southwestern edge of the shell (hereafter SW-edge) shows the highest value of $R_{12\text{CO}32/13\text{CO}21} \sim 20$, where the radio continuum shell is strongly deformed. On the other hand, the 40 km s^{-1} cloud shows no significant enhancement of $R_{12\text{CO}32/13\text{CO}21}$ toward the SNR shell. The southeast shell in the 60 km s^{-1} cloud also shows higher values of $R_{12\text{CO}32/13\text{CO}21}$, while the regions with high-intensity ratios continuously extend beyond the radio-shell boundary and may not be related to W49B.

3.5. Physical conditions of the molecular clouds

To reveal physical conditions for each cloud in detail, we performed the Large Velocity Gradient (LVG) analysis (e.g., Goldreich & Kwan 1974; Scoville & Solomon 1974). The LVG analysis can calculate the radiative transfer of molecular line emission, assuming a spheri-

cally isotropic cloud with uniform photon escape probability, temperature, and radial velocity gradient of dv/dr . Here, dv is the half-width half-maximum of CO line profiles and dr is a cloud radius. We selected six individual CO peaks for each cloud, which are significantly detected both the ^{12}CO and ^{13}CO emission lines. Four of them appear to be along the radio continuum shell or filaments (hereafter refer to as “shell clouds”), and the others were selected as reference which are located outside of the shell (hereafter refer to as “reference clouds”). CO spectra toward each position are shown in Figure 6. We adopt $dv/dr = 2.5 \text{ km s}^{-1} \text{ pc}^{-1}$ for the 10 km s^{-1} SW-shell and the 40 km s^{-1} SE-shell; $1.5 \text{ km s}^{-1} \text{ pc}^{-1}$ for the 60 km s^{-1} SW-edge, NW-shell, and Reference-SW; and $1.0 \text{ km s}^{-1} \text{ pc}^{-1}$ for the others. We also utilized the abundance ratio of $[^{12}\text{CO}/\text{H}_2] = 5 \times 10^{-5}$ (Blake et al. 1987) and the isotope abundance ratio of $[^{12}\text{CO}/^{13}\text{CO}] = 49$ (Langer & Penzias 1990).

Figure 7 shows the LVG results on the number density of molecular hydrogen, $n(\text{H}_2)$, and the kinematic temperature, T_{kin} , toward the six positions for each cloud. The best-fit values of $n(\text{H}_2)$ and T_{kin} are summarized in Table 1. In the 10 km s^{-1} cloud, we find that the

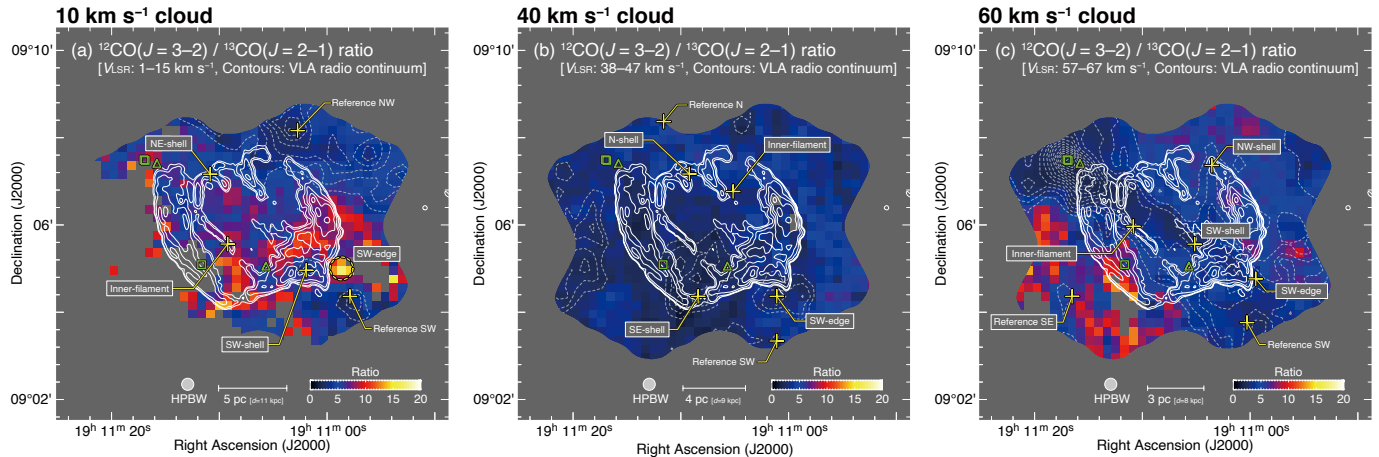


Figure 5. Intensity ratio maps of $^{12}\text{CO}(J=3-2) / ^{13}\text{CO}(J=2-1)$ for (a) the 10 km s^{-1} cloud, (b) the 40 km s^{-1} cloud, and (c) the 60 km s^{-1} cloud. Each data was smoothed to match the beam size $16''6$. The velocity range of each cloud and superposed solid contours are the same as shown in Figure 1. Superposed dashed contours indicate $^{13}\text{CO}(J=2-1)$ integrated intensities, whose lowest contour levels are 3 K km s^{-1} and contour intervals are 1.0 K km s^{-1} for the 10 km s^{-1} cloud; 0.5 K km s^{-1} for the 40 km s^{-1} cloud; and 1.5 K km s^{-1} for the 60 km s^{-1} cloud. The gray areas represent that the $^{12}\text{CO}(J=3-2)$ and/or $^{13}\text{CO}(J=2-1)$ data show the lower significance than $\sim 7\sigma$. Yellow crosses (Reference SW/NW, SW/NE-shell, central-filament) and a dashed circle (SW-edge) discussed in Section 3.5 are indicated. Green squares and triangles also indicate the positions of H II regions and IRAS point sources, respectively (Beichman et al. 1988; Urquhart et al. 2009).

shell clouds show $T_{\text{kin}} \sim 20\text{--}60 \text{ K}$, which are significantly higher than that of the reference clouds ($T_{\text{kin}} = 15 \text{ K}$). By contrast, all shell clouds in both the 40 km s^{-1} and 60 km s^{-1} components show $T_{\text{kin}} \sim 10 \text{ K}$ which are roughly consistent with their reference clouds except for Reference-SE in the 60 km s^{-1} ($T_{\text{kin}} = 21 \text{ K}$). We also note that there is no relation between the number density of molecular hydrogen and kinetic temperature for each cloud.

4. DISCUSSION

4.1. Molecular Clouds Associated with W49B

Previous studies proposed three candidates of molecular clouds which are interacting with the SNR W49B: namely the 10 km s^{-1} cloud, 40 km s^{-1} cloud, and the 60 km s^{-1} cloud (Zhu et al. 2014; Kilpatrick et al. 2016; Lee et al. 2020). Their claim is mainly based on three elements: (1) a line-broadening feature of CO emission at $\sim 10 \text{ km s}^{-1}$, (2) a wind-bubble like morphology of CO cloud at $\sim 40 \text{ km s}^{-1}$, and (3) a central velocity of shocked H_2 line emission at $\sim 64 \text{ km s}^{-1}$. In this section, we discuss which cloud is the most likely to be associated with W49B in terms of spatial distributions, presence of the expanding gas motion, and physical conditions of CO clouds.

4.1.1. Spatial Distributions of CO Clouds

We first emphasize that the 10 km s^{-1} cloud shows a clear spatial correspondence with the radio continuum shell and filaments (see Figure 3 and Section 3.2). In particular, a majority of CO clouds at $\sim 10 \text{ km s}^{-1}$ are located along the outer boundary of the radio continuum shell: ^{13}CO clouds in the northern shell at $6.6\text{--}9.4$

km s^{-1} , and arc-like ^{12}CO clouds in the southwestern shell at $12.2\text{--}15.0 \text{ km s}^{-1}$. Moreover, ^{13}CO clumps at $3.8\text{--}9.4 \text{ km s}^{-1}$ spatially coincide well with radio filaments inside the shell. Such spatial correspondence is naturally expected as a result of shock-cloud interactions. According to magneto-hydrodynamical (MHD) simulations, interactions between supernova shocks and clumpy clouds enhance turbulent magnetic field up to $\sim 1 \text{ mG}$ on the surface of shocked clouds, where the synchrotron radio/X-ray radiation becomes brighter (Inoue et al. 2009, 2012; Celli et al. 2019). This was further supported by several observations toward the Galactic and Magellanic SNRs (Sano et al. 2013, 2017a,b, 2019b, 2020b; Yamane et al. 2018; Kuriki et al. 2018), and hence it should not be surprising that shock-cloud interactions with the magnetic field amplification occurred in W49B as well.

However, we cannot rule out the possibility of shock-interaction with the 40 km s^{-1} and 60 km s^{-1} clouds from the spatial comparative studies alone. In fact, molecular clouds at $38.0\text{--}40.0 \text{ km s}^{-1}$ and $42.0\text{--}44.0 \text{ km s}^{-1}$ show good spatial correspondences with the southeastern half and southwestern shell of the SNR, respectively (see Figure 3). The $63.0\text{--}65.0 \text{ km s}^{-1}$ CO map also shows a good anti-correlation with the radio shell, which is not inconsistent with the picture of magnetic field amplification via the shock-cloud interaction.

4.1.2. Shock and Wind Induced Expanding Gas Motion

We argue that the cavity-like structures in the position-velocity diagrams at the 10 km s^{-1} and 40 km s^{-1} clouds provide further supports for the shock interactions (see Figures 4a–4d). Because such cavity-like

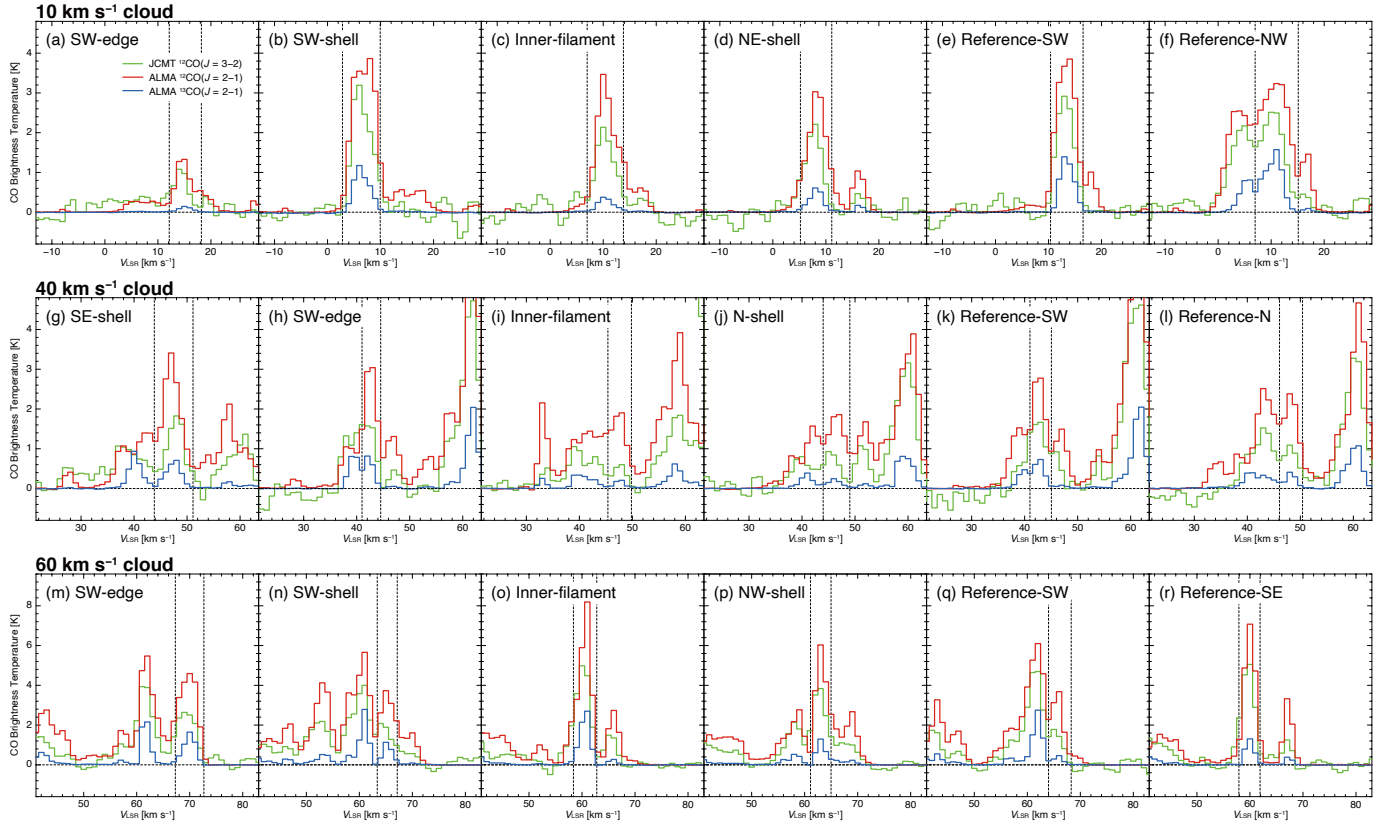


Figure 6. CO intensity profiles toward individual CO peaks in (a–f) the 10 km s^{-1} cloud, (g–l) the 40 km s^{-1} cloud, and (m–r) the 60 km s^{-1} cloud. The CO spectra enclosed by vertical lines represent individual CO peaks that are focused on the present study. Each CO data was smoothed to match the beam size $16''.6$ and the velocity resolution of 1 km s^{-1} . In SW-edge spectra of the 10 km s^{-1} cloud, we combined four pixels around the highest intensity ratio of $^{12}\text{CO}(J=3-2) / ^{13}\text{CO}(J=2-1)$ as shown in Figure 5a.

structure toward a SNR indicates an expanding gas motion, which is thought to be formed by a combination of shock acceleration and strong gas winds from the progenitor system: stellar winds from a high-mass progenitor or disk winds from a progenitor system of post single-degenerate explosion. In the present study, an expanding velocity ΔV is derived to be $\sim 6 \text{ km s}^{-1}$ for the 10 km s^{-1} cloud; and $\sim 3 \text{ km s}^{-1}$ for the 40 km s^{-1} cloud. These values are roughly consistent with other Galactic/Magellanic SNRs (e.g., Koo et al. 1990; Koo & Heiles 1991; Sano et al. 2017b, 2019c; Kuriki et al. 2018).

It is noteworthy that the two expanding cavities are independent because their ΔV values are much smaller than the velocity difference of the 10 km s^{-1} and 40 km s^{-1} clouds. Therefore, either expanding shell is located at the same distance with W49B, and the forward shock has been impacted the wind-cavity wall where the shock–cloud interaction occurred. The other expanding shell is likely not associated with W49B. According to Sofue (2020), there are many relics of fully evolved SNRs in the Galactic plane that cannot be observed by radio continuum, optical, infrared, and X-rays. Because

thermal radiation from SNRs has shorter cooling time (below $\sim 10 \text{ kyr}$) than the lifetime of giant molecular clouds ($\sim 10 \text{ Myr}$, e.g., Fukui et al. 1999; Kawamura et al. 2009). The expanding gas motion of the 10 km s^{-1} or 40 km s^{-1} cloud is therefore likely one of such objects that happen to be located along the line of sight.

4.1.3. Kinetic Temperature of Molecular Clouds

According to the LVG analysis in Section 3.5, the higher kinetic temperature $T_{\text{kin}} \sim 20\text{--}60 \text{ K}$ of the shell clouds are seen in the 10 km s^{-1} cloud, suggesting that shock-heating likely occurred. Because the T_{kin} values are roughly consistent with the previous studies of shock-heated molecular clouds in the vicinity of middle-aged SNRs (e.g., Seta et al. 1998; Gusdorf et al. 2012; Yoshiike et al. 2013; Anderl et al. 2014; Dell’Ova et al. 2020). In addition, the presence of high temperature dust components of $45 \pm 4 \text{ K}$ and $151 \pm 20 \text{ K}$ also support the shock-heating scenario (Zhu et al. 2014). Moreover, the bright 24-micron emission is detected in the southwestern shell where SW-edge of the 10 km s^{-1} cloud shows the highest kinetic temperature of $\sim 60 \text{ K}$. It is noteworthy that there are no other extra heating sources

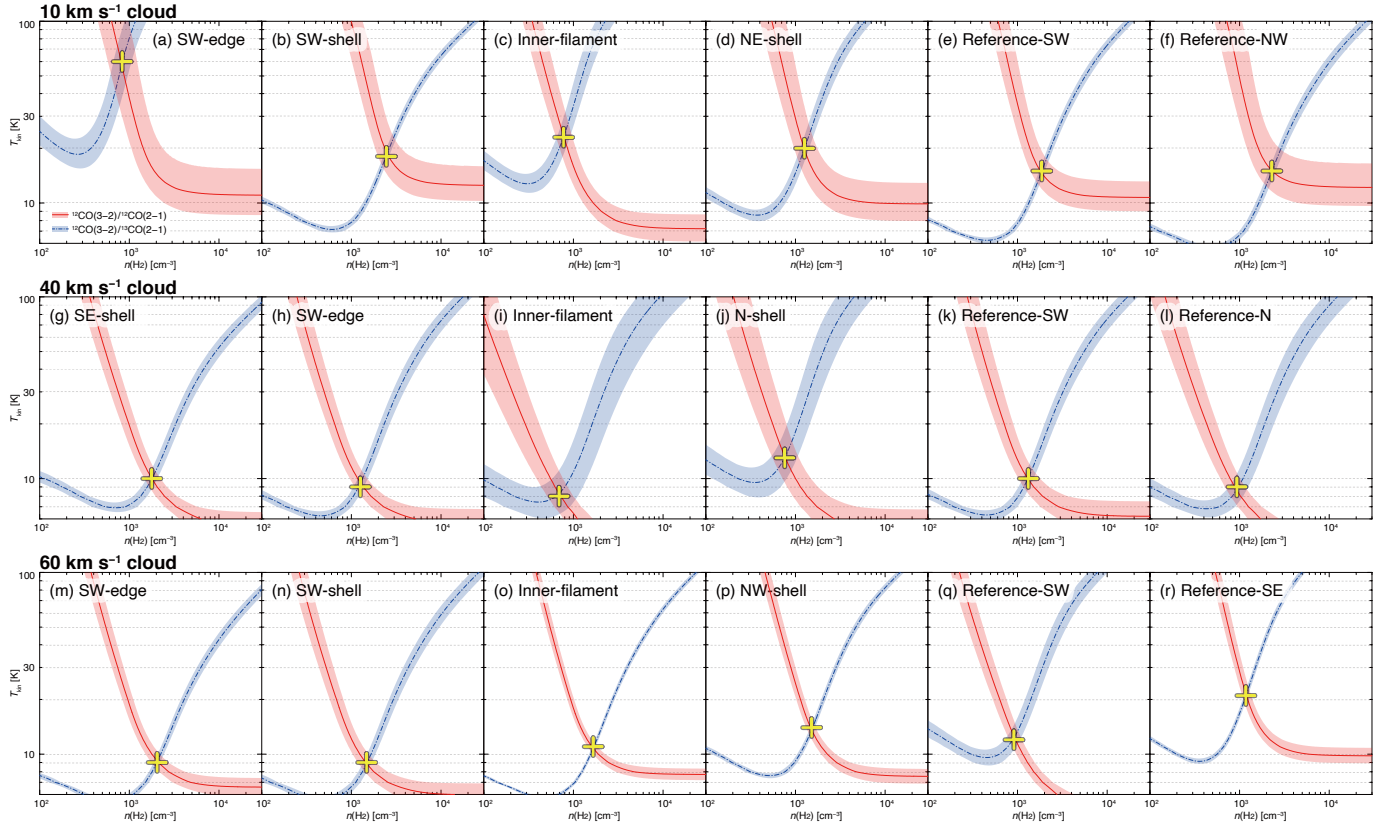


Figure 7. LVG results on the number density of molecular hydrogen, $n(\text{H}_2)$, and the kinetic temperature, T_{kin} for each cloud as shown in Figure 6. The red lines and blue dash-dotted lines indicate the intensity ratios of $^{12}\text{CO}(J=3-2)/^{12}\text{CO}(J=2-1)$ and $^{12}\text{CO}(J=3-2)/^{13}\text{CO}(J=2-1)$, respectively. The shaded areas in red and blue represent 1σ error ranges of each intensity ratio. Yellow crosses indicate the best-fit values of $n(\text{H}_2)$ and T_{kin} for each cloud. The results are summarized in Table 1.

such as IRAS point sources or H II regions toward the shell clouds (see also Figure 5).

By contrast, all shell clouds in the 40 km s^{-1} and 60 km s^{-1} components show $T_{\text{kin}} \sim 10$ K, implying quiescent molecular clouds without any extra-heating processes such as shock heating and stellar radiation. Interestingly, Reference-SE in the 60 km s^{-1} cloud shows warmer temperature of ~ 20 K, despite the reference cloud is far from the SNR shell. A possible scenario is that a part of the 60 km s^{-1} cloud is located at the tangent point of the Galaxy, and hence the velocity crowding would accumulate diffuse gas and increase the ambient gas temperature (e.g., Liu et al. 2019). In any case, there is no shock-heated gas in both the 40 km s^{-1} and 60 km s^{-1} clouds.

4.1.4. Final Decision and Consistency with Previous Studies

In conclusion, we claim that the 10 km s^{-1} cloud is the one most likely associated with W49B in terms of its spatial distribution, kinetics, and physical conditions. This velocity is consistent not only with the line-broadening measurements by Kilpatrick et al. (2016), but also with the latest H I absorption measurement toward W49B by

Ranasinghe & Leahy (2018). In this case, the kinematic distance of W49B is slightly revised to 11.0 ± 0.4 kpc assuming the Galactic rotation curve model of Brand & Blitz (1993) and the latest Galactic parameters of $R_0 = 7.92$ kpc and $\Theta_0 = 227$ km s^{-1} (VERA Collaboration et al. 2020). This value is also roughly consistent with the previous distance to W49B of 11.3 ± 0.4 kpc derived by H I absorption (Ranasinghe & Leahy 2018).

On the other hand, there is large gap in radial velocities between the 10 km s^{-1} cloud and shocked H_2 line emission at ~ 64 km s^{-1} (Lee et al. 2020). We argue that this inconsistency should not be a problem considering the excitation condition for each line emission. In general, the CO line emission at 2.6 mm (also known as $^{12}\text{CO } J=1-0$ transition line) can trace a bulk mass of molecular cloud with low kinetic temperature of ~ 10 K. On the other hand, the supernova-shocked H_2 line emission traces only a small portion of molecular cloud which is highly excited into ~ 2000 – 3000 K (e.g., Mouri 1994; Lee et al. 2020). In W49B, the CO-traced molecular cloud mass is $\sim 2.7 \times 10^4 M_\odot$ for the 10 km s^{-1} cloud, whereas the mass of shocked H_2 is only 14–550 M_\odot (Keohane et al. 2007). This indicates that the shocked H_2 mass is only $\sim 2\%$ of the CO-traced molec-

Table 1. Results of LVG analysis at the 10 km s⁻¹, 40 km s⁻¹, and 60 km s⁻¹ clouds

Name	¹² CO		¹³ CO	$n(\text{H}_2)$ ($\times 10^3 \text{ cm}^{-3}$)	T_{kin} (K)
	$J = 3-2$	$J = 2-1$	$J = 2-1$		
	(K)	(K)	(K)		
(1)	(2)	(3)	(4)	(5)	(6)
<u>10 km s⁻¹ cloud</u>					
SW-edge	1.02	1.35	0.14	$0.83^{+0.10}_{-0.05}$	60^{+47}_{-26}
SW-shell	3.12	3.97	1.12	$2.45^{+0.50}_{-0.16}$	18^{+7}_{-3}
Inner-filament	2.06	3.25	0.37	$0.78^{+0.03}_{-0.02}$	23^{+9}_{-5}
NE-shell	2.16	2.96	0.60	$1.26^{+0.15}_{-0.09}$	20^{+8}_{-4}
Reference-SW	3.02	4.03	1.43	$1.86^{+0.14}_{-0.08}$	15^{+3}_{-2}
Reference-NW	2.49	3.19	1.41	$2.29^{+0.46}_{-0.20}$	15^{+6}_{-3}
<u>40 km s⁻¹ cloud</u>					
SE-shell	1.81	3.32	0.68	$1.78^{+0.08}_{-0.00}$	10^{+2}_{-1}
SW-edge	1.78	3.13	2.40	$1.26^{+0.03}_{-0.03}$	9^{+2}_{-1}
Inner-filament	0.64	1.91	0.22	$0.69^{+0.02}_{-0.00}$	8^{+3}_{-2}
N-shell	0.93	5.22	0.23	$0.76^{+0.05}_{-0.02}$	13^{+6}_{-3}
Reference-SW	1.65	2.83	0.77	$1.32^{+0.09}_{-0.09}$	10^{+2}_{-2}
Reference-N	1.05	2.40	0.42	$0.93^{+0.03}_{-0.00}$	9^{+2}_{-2}
<u>60 km s⁻¹ cloud</u>					
SW-edge	2.78	4.61	1.62	$2.04^{+0.05}_{-0.04}$	9^{+1}_{-1}
SW-shell	2.09	3.66	1.19	$1.48^{+0.03}_{-0.03}$	9^{+1}_{-1}
Inner-filament	5.22	7.93	2.82	$1.66^{+0.08}_{-0.04}$	11^{+1}_{-1}
NW-shell	3.98	6.13	1.31	$1.51^{+0.04}_{-0.03}$	14^{+1}_{-2}
Reference-SW	1.76	3.64	0.42	$0.91^{+0.02}_{-0.00}$	12^{+3}_{-1}
Reference-SE	5.20	7.15	1.33	$1.17^{+0.06}_{-0.02}$	21^{+3}_{-2}

NOTE—Col. (1): Region name for each cloud. Cols. (2)–(3): Radiation temperature for each line emission derived by the least-squares fitting using a single Gaussian function. Col. (4): Number density of molecular hydrogen. Col. (5): Kinetic temperature.

ular cloud mass at most. Considering the momentum conservation between the SNR shocks and interacting clouds, the shocked H₂ component is more easily accelerated than the CO-traced molecular cloud. We therefore argue that the velocity inconsistency between the CO cloud and shocked H₂ component is caused by the difference of their excitation conditions and masses.

In any case, the physical interaction of the 10 km s⁻¹ cloud with W49B means that the bulk mass of molecular clouds is concentrated in the northwestern half of W49B, not in the southwest shell. This is consistent with the hydrogen density maps derived by Zhou & Vink (2018), who found higher plasma densities in the west of W49B by the X-ray spectral modeling. The inhomogeneous gas distribution will significantly affect to understand the origins of recombining plasma and gamma-rays from W49B. We will discuss later them the latter Sections 4.3 and 4.4.

4.2. A Detailed Comparison with X-Rays

To reveal a physical relation between the 10 km s⁻¹ cloud and X-ray radiation, we here compare the CO dis-

tributions with *Chandra* X-ray images². Figure 8a shows the ALMA ACA ¹²CO($J = 2-1$) integrated intensity overlaid with the *Chandra* X-ray contours at the energy band of 2–7 keV. In the integration velocity range of 12.2–15.0 km s⁻¹, CO clouds are perfectly along with the zigzag pattern of the western X-ray shell, indicating that the shock ionization occurred. Note that the spatial correspondence is also seen in the X-ray image at 4.2–5.5 keV, which are mostly free from the interstellar absorption. We thus suggest that the shockwave was strongly decelerated and deformed in the western shell along the dense clouds, whereas the eastern shell was freely expanded with a smooth shape of the forward shock. This also indicates that the shock velocity of the eastern shell is faster than that of the western shell. Fur-

² Because the shell boundary of X-rays is almost similar to that of radio continuum except for the western half, we here only present a spatial comparison with the CO map of 12.2–15.0 km s⁻¹ which is bright in the western part of the shell.

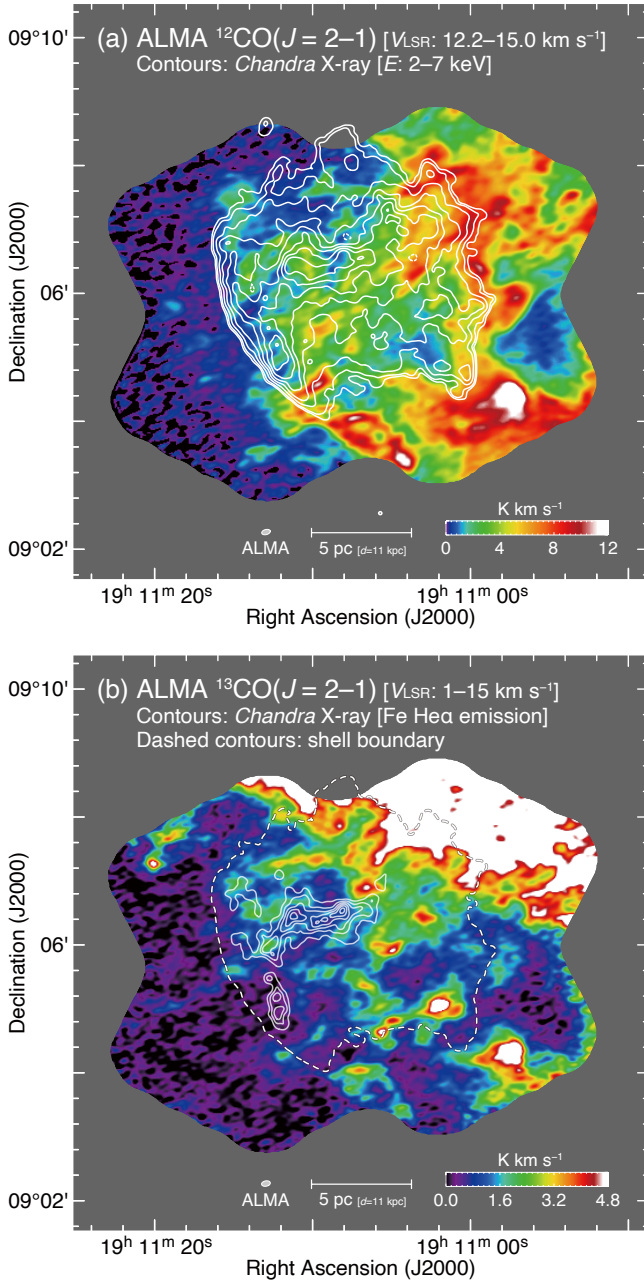


Figure 8. (a) Integrated intensity maps of ALMA ACA $^{12}\text{CO}(J=2-1)$ superposed on the *Chandra* X-ray intensity contours in the energy band of 2–7 keV. The integration velocity range of CO is from 12.2 to 15.0 km s $^{-1}$. The contour levels are 0.3, 0.4, 0.7, 1.2, 1.9, 2.8, 3.9, and 5.2×10^{-7} photon cm $^{-2}$ s $^{-1}$. (b) Integrated intensity maps of ALMA ACA $^{13}\text{CO}(J=2-1)$ superposed on the continuum-subtracted Fe He α emission. The integration velocity range of CO is from 1.0 to 15.0 km s $^{-1}$. The contour levels are 0.5, 0.8, 1.1, 1.4, 1.7, and 2.0×10^{-7} photon cm $^{-2}$ s $^{-1}$.

ther proper motion studies might be able to reveal the velocity difference in the east–west direction.

Figure 8b shows an overlay map of the $^{13}\text{CO}(J=2-1)$ intensity image and the continuum-subtracted Fe He α emission in white contours. To compare the Fe-rich ejecta with the total amount of dense clouds, we use ^{13}CO with the whole velocity range of 1.0–15.0 km s $^{-1}$. Although the elongated structure of Fe-rich ejecta is believed to be related to a bipolar/jet-driven Type Ib/Ic explosion (Keohane et al. 2007; Lopez et al. 2013a), the Fe-rich ejecta is mainly located on the void of dense molecular clouds. Moreover, almost Fe-rich ejecta is surrounded by dense molecular clumps. We argue that this situation is consistent with the supernova explosion inside a barrel-shaped cavity which was proposed by Zhou & Vink (2018). The authors revealed that an enhancement of cool plasma component along the Fe-rich ejecta (or the void of dense clouds) was observed by a spatially resolved X-ray spectroscopy (see Figure 4 in Zhou & Vink 2018). Following the proposed scenario, the forward shock was freely expanded in the low-density medium at the beginning, and then suddenly encountered with the dense gaseous materials traced by ^{13}CO line emission and/or cool plasma component. Since the shock–cloud interaction generates multiple reflected (or inward) shocks, the Fe-rich ejecta is efficiently heated up at higher densities toward the center of the SNR (see also Sano et al. 2019b). The X-Ray Imaging and Spectroscopy Mission (XRISM, XRISM Science Team 2020) will provide us with further understanding of shock-interactions through a detailed spatial comparison between the X-ray derived ionic properties and CO clouds.

4.3. Origin of the High-Temperature Recombining Plasma in W49B

It is a long-standing question how the recombining (overionized) plasma is formed in SNRs since its discovery in 2002 (IC443, Kawasaki et al. 2002). Subsequent detailed X-ray spectroscopic observations revealed that nearly 20 SNRs show the overionized state (e.g., W49B, Ozawa et al. 2009; G359.1–0.5, Ohnishi et al. 2011; W28, Sawada & Koyama 2012; W44, Uchida et al. 2012; G346.6–0.2, Yamauchi et al. 2013; 3C 391, Ergin et al. 2014; CTB 37A, Yamauchi et al. 2014; G290.1–0.8, Kamitsukasa et al. 2015; LMC N49, Uchida et al. 2015; Kes 17, Washino et al. 2016; G166.0+4.3, Matsumura et al. 2017a; 3C400.2, Ergin et al. 2017; LMC N132D, Bamba et al. 2018; HB21, Suzuki et al. 2018; CTB1, Katsuragawa et al. 2018; Sagittarius A East, Ono et al. 2019; G189.6+3.3, Yamauchi et al. 2020, see also a review by Yamaguchi 2020). However, the physical origin of recombining plasmas is still under debate.

Since the recombining plasma is characterized by higher ionization temperature kT_i than the electron temperature kT_e , rapid electron cooling or increasing ionization state is needed to produce the plasma state. Three scenarios have been proposed to explain the origin of recombining plasmas in SNRs, called adiabatic cooling, thermal conduction, and photoionization scenarios. In

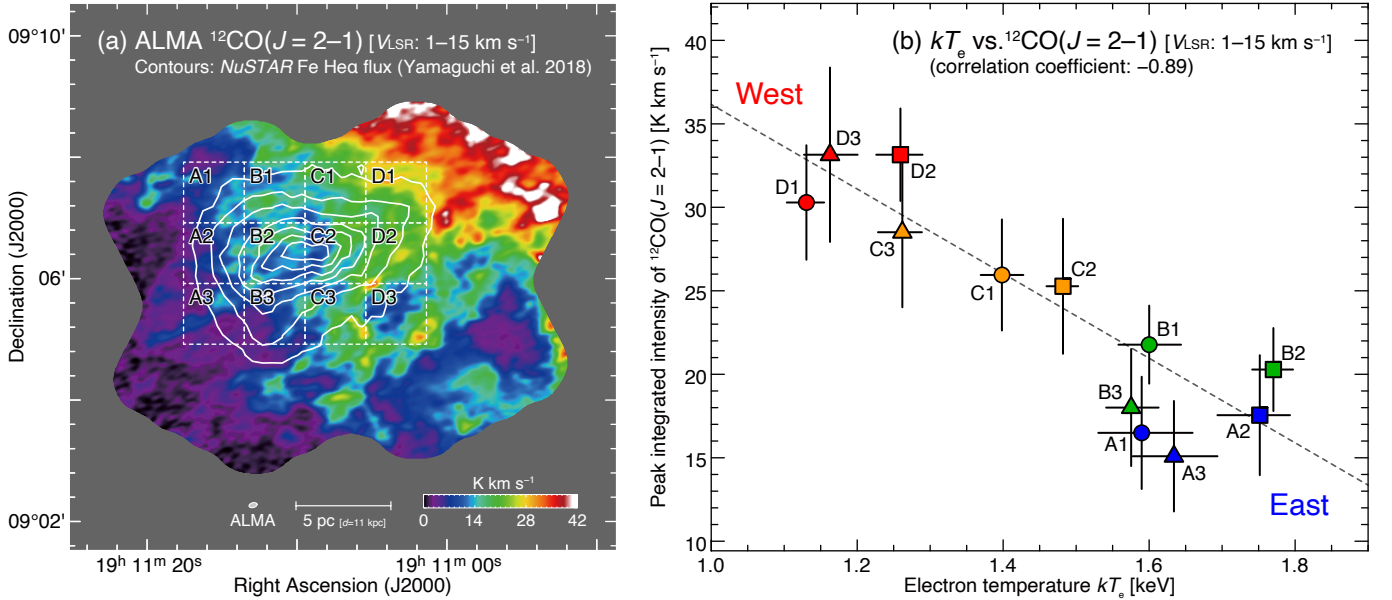


Figure 9. (a) Integrated intensity maps of ALMA ACA $^{12}\text{CO}(J = 2-1)$ for the 10 km s^{-1} cloud superposed on *NuSTAR* Fe He α flux contours (Yamaguchi et al. 2018). The integration velocity range and contour levels are the same as shown in Figures 2a and 6, respectively. The bashed 12 boxes indicate $1' \times 1'$ regions used for the spatially resolved spectral analysis in Yamaguchi et al. (2018) and deriving CO averaged integrated intensities in Figure 9b. (b) Scatter plot between the electron temperature kT_e (Yamaguchi et al. 2018) and peak integrated intensities of $^{12}\text{CO}(J = 2-1)$ for box regions A1–3, B1–3, C1–3, and D1–3 as shown in Figure 9a. Error bars of CO and kT_e represent standard deviation of CO integrated intensity and 1σ confidence level for each box region. The dashed line indicates the linear regression applying the least squares method.

the adiabatic cooling (a.k.a. rarefaction) scenario, rapid electron cooling occurs when the shockwaves breakout from a dense ISM (e.g., CSM) into a much less dense medium (e.g., Itoh & Masai 1989; Masai 1994; Yamaguchi et al. 2018). In the thermal conduction scenario, such rapid electron cooling is caused by interactions between the shockwaves and cold dense clouds through thermal conduction (e.g., Kawasaki et al. 2002; Matsumura et al. 2017a,b; Okon et al. 2018, 2020). On the other hand, the photoionization scenario proposes that an external X-ray radiation or low-energy CRs increase the ionization state via photoionization (e.g., Nakashima et al. 2013; Ono et al. 2019; Hirayama et al. 2019). Because photoionization can be seen in limited environments such as near the Galactic center or a SNR with strong Fe I $K\alpha$ emission, the adiabatic cooling and thermal conduction scenarios are thought to be the formation mechanisms of recombining plasmas in most SNRs.

The origin of recombining plasma in W49B has been discussed in the past decade. The thermal conduction scenario was initially proposed by Kawasaki et al. (2005), whereas the adiabatic cooling scenario is more favored in the subsequent studies (Miceli et al. 2010; Lopez et al. 2013a; Zhou et al. 2011; Yamaguchi et al. 2018). Because the recombining plasma in W49B shows a positive correlation between the ionization timescale $n_e t$ and kT_e . Further, there is no correlation between the plasma condition and ambient clouds traced by near in-

frared emission (Yamaguchi et al. 2018). This trend is in contrast to what is observed in W44 (see also Okon et al. 2020 and a review in Yamaguchi 2020). On the other hand, most recent X-ray studies presented that the X-ray spectra from W49B are reproduced by two ejecta components (low- and high-temperature plasma). The authors proposed thermal conduction scenarios especially for the high-temperature recombining plasma in W49B, considering the conduction timescale (Sun & Chen 2020; Holland-Ashford et al. 2020). Note that Holland-Ashford et al. (2020) argued that thermal conduction is a possible origin of recombining plasma in the eastern regions of W49B because dense molecular clouds are thought to be associated in the southwestern shell (Keohane et al. 2007; Zhu et al. 2014). In this section, we argue that the origin of the high-temperature recombining plasma in W49B can be understood as the thermal conduction scenario considering the CO-traced interacting molecular clouds in W49B.

Figure 9a shows the $^{12}\text{CO}(J = 2-1)$ integrated intensity map of the 10 km s^{-1} cloud superposed on the *NuSTAR* Fe He α flux contours (Yamaguchi et al. 2018). The twelve $1' \times 1'$ boxes indicate regions used for spatially resolved spectral analysis using *NuSTAR* by Yamaguchi et al. (2018). The authors fitted X-ray spectra above 3 keV using a single temperature model, because the energy band is dominated by the high-temperature plasma. We note that the CO integrated intensities are significantly changed region to region, which shows an

Table 2. Comparison of Physical Properties in Eleven Gamma-Ray SNRs

Name	Distance	Diameter	Age	n_p	W_p	References
(1)	(kpc)	(pc)	(kyr)	(cm^{-3})	(10^{49} erg)	(7)
RX J1713.7–3946	1.0	18	1.6	130	$0.16_{-0.08}^{+0.07}$	Fukui et al. (2012)
RX J0852.0–4622	0.75 ^a	24	1.7 ^a	100	$0.07_{-0.02}^{+0.02}$	Fukui et al. (2017)
RCW 86	2.5	30	1.8	75	$0.11_{-0.01}^{+0.01}$	Sano et al. (2019a)
HESS J1731–347	5.7	44	4.0	60	$0.66_{-0.22}^{+0.22}$	Fukuda et al. (2014)
G39.2–0.3	6.2	14	$5.0_{-2.0}^{+2.0\text{b}}$	400	$3.2_{-0.8}^{+1.1}$	de Oña Wilhelmi et al. (2020)
W49B	11.0	16	$6.0_{-1.0}^{+1.0\text{c}}$	650	$2.1_{-0.6}^{+1.1}$	This work
Kes 79	5.5	16	$8.3_{-0.5}^{+0.5}$	360	0.5	Kuriki et al. (2018)
W44	3.0 ^d	27	20.0 ^e	200	1.0	Yoshiike et al. (2013)
IC443	1.5 ^f	20	$25.0_{-5.0}^{+5.0\text{g}}$	680	0.09	Yoshiike et al. (2021)
LMC N132D	50.0	25	$2.5_{-0.2}^{+0.2\text{h}}$	< 2000	> 0.5	Sano et al. (2020a)
LMC N63A	50.0	18	$3.5_{-1.5}^{+1.5\text{i}}$	190	$0.9_{-0.6}^{+0.5}$	Sano et al. (2019b)

NOTE—Col. (1): Name of SNRs. Col. (2): Distance to SNRs in units of kpc. Col. (3): Diameter of SNRs in units of pc. Col. (4): Age of SNRs in units of kyr. Col. (5): Averaged number density of total interstellar protons n_p in units of cm^{-3} . Col. (6): Total energy of cosmic-ray protons W_p in units of 10^{49} erg. Col. (7): References for CO/H I derived n_p and W_p for each SNR. Other specific references are also shown as follows: ^aKatsuda et al. (2008), ^bSu et al. (2011), ^cZhou & Vink (2018), ^dCaswell et al. (1975), ^eWolszczan et al. (1991), ^fWelsh & Sallmen (2003), ^gLee et al. (2008); Olbert et al. (2001), ^hLaw et al. (2020), and ⁱHughes et al. (1998).

intensity gradient from the southeast to the northwest as mentioned in Section 3.

Figure 9b shows a scatter plot between kT_e of the high-temperature recombining plasma (Yamaguchi et al. 2018) and peak integrated intensity of $^{12}\text{CO}(J = 2-1)$ line emission for each box. We find a clear negative correlation between the two. More precisely, kT_e values in high-temperature plasma are increasing from the west (cloud rich) regions to the east (cloud poor) regions. This is consistent with the thermal conduction scenario: rapid electron cooling occurred in cold/dense cloud rich regions. Note that this finding will not rule out the adiabatic cooling scenario in W49B. In fact, the X-ray spectra from W49B are reproduced two ejecta components: the low-temperature recombining plasma favors the adiabatic cooling scenario whereas the high-temperature component is likely produced by the thermal conduction (Sun & Chen 2020; Holland-Ashford et al. 2020). In other words, both the thermal conduction and adiabatic cooling processes coexist in W49B.

Finally, we discuss the reason why our conclusion—the thermal conduction origin of the high-temperature plasma—is different from some previous studies. One of the most important issues is the previous evaluation of the ISM interacting with W49B. Almost all previous studies used the shocked H_2 distribution as the bulk mass of the ISM. However, as discussed in Section 4.1.4, the shocked H_2 mass is only $\sim 2\%$ of the CO-traced molecular cloud mass. Because the shocked H_2 map is bright in the southeast, most of researchers believed that the southeast shell is interacting with dense molec-

ular clouds and the ISM mass of east is higher than that of west. Some previous studies therefore concluded that the lower plasma temperature in west was caused by the adiabatic cooling process (e.g., Holland-Ashford et al. 2020; Yamaguchi et al. 2018). By contrast, it is noteworthy that Zhou & Vink (2018) suggested that molecular cloud density is higher in the west than the east, which is compatible with our ALMA results. We also note there are different interpretations for the $n_e t$ variation in the high-temperature plasma. Yamaguchi et al. (2018) used $n_e t$ as a proxy for electron density, assuming a uniform time since heating and uniform initial temperature. The former contrasts with the results of Holland-Ashford et al. (2020) and Zhou & Vink (2018), who found higher recombination ages in the east than the west. The positive correlation between $n_e t$ and kT_e in W49B may have to be reconsidered. In any case, we emphasize that the proper evaluation of the ISM surrounding an SNR is essential to understand the origin of recombining plasma correctly. Further detailed comparative studies of CO based molecular cloud properties and X-ray spectroscopic results are needed to better understand the origin of recombining plasma in SNRs.

4.4. Total Energy of Cosmic-Ray Protons

It is a hundred-year problem how CRs, mainly comprising relativistic protons, are accelerated in interstellar space. SNRs are believed to be acceleration sites for Galactic CRs below ~ 3 PeV through the diffusive shock acceleration (DSA, e.g., Bell 1978; Blandford & Ostriker 1978). A conventional value of the total energy

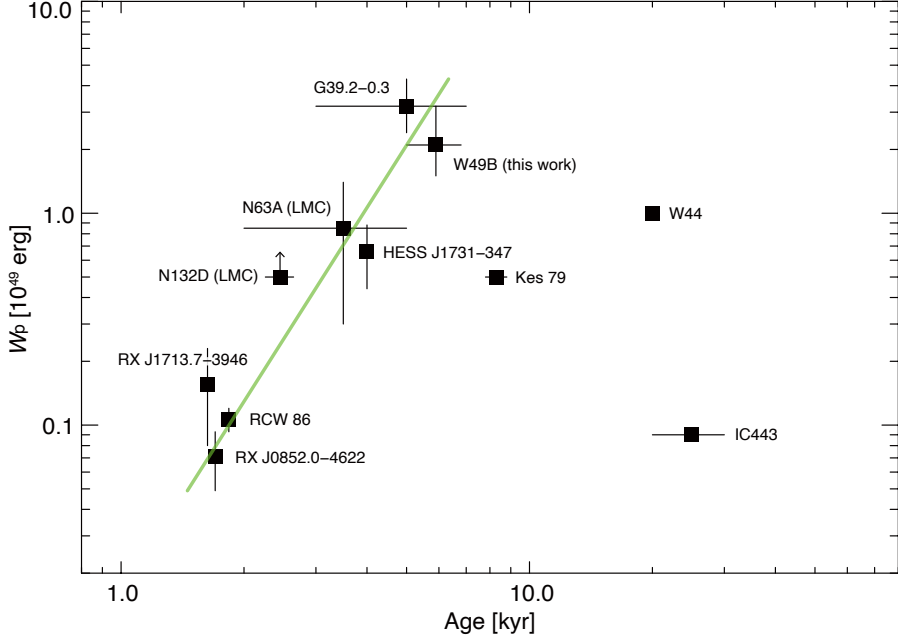


Figure 10. Scatter plot between the age of SNRs and the total energy of cosmic-ray protons W_p . The data points and references are summarized in Table 2. The green solid line indicates the linear regression of the double-logarithmic plot applying the least squares method.

of CRs accelerated in an SNR is thought to be $\sim 10^{49}$ – 10^{50} erg, corresponding to ~ 1 – 10% of typical kinematic energy released by a supernova (10^{51} erg, e.g., Gabici 2013; Leahy et al. 2019). One of the foremost challenges is to validate these predictions experimentally.

Gamma-ray and radio-line observations hold a key to understand the acceleration of CRs in SNRs. Gamma-rays from SNRs are produced by two different mechanisms: hadronic and leptonic processes (e.g., Aharonian et al. 1994; Drury et al. 1994). For the hadronic process, CR proton–interstellar proton interaction creates a neutral pion that quickly decays into two gamma-ray photons (hadronic gamma-ray). For the leptonic scenario, a CR electron energizes a low-energy photon into gamma-ray energy via inverse Compton scattering, in addition to produce gamma-rays through non-thermal Bremsstrahlung (leptonic gamma-ray). To confirm the acceleration of relativistic protons, the main component of CRs, it is crucial to detect the characteristic spectral feature of hadronic gamma-rays with a cut-off at a few GeV known as pion-decay bump (e.g., Giuliani et al. 2011; Ackermann et al. 2013). In addition, a good spatial correspondence between gamma-rays and interstellar protons provides an alternative support for the CR proton acceleration (e.g., Fukui et al. 2003, 2012, 2017; Aharonian et al. 2008; Yoshiike et al. 2013; Sano et al. 2019a), because the hadronic gamma-ray flux is proportional to the total energy of CR protons and the number density of interstellar protons. Note that the interstellar protons are mainly either neutral molecular and atomic hydrogen traced by CO and H I radio-

lines, respectively. Adopting the number density of targeted interstellar protons, the total energy of CR protons was estimated to be $W_p \sim 10^{48}$ – 10^{49} erg toward a dozen gamma-ray SNRs. However, it is still under debate which parameters are important to understand the variety of observed (or in-situ) W_p values. To better understand the origins of CR protons and variety of W_p , we need more samples as well as detailed gamma-ray and radio-line studies for SNRs.

W49B is thought to be one of the CR proton accelerators because of the detection of hadron-dominant gamma-rays with a pion-decay bump (H. E. S. S. Collaboration et al. 2018). In fact, the best-fit position of GeV gamma-ray detected by *Fermi* Large Area Telescope (LAT) is the edge of the SE shell, where the bright radio continuum, shocked H_2 emission, and the dense molecular clouds are located. To obtain the total energy of CR protons in W49B, we first estimate the number density of interstellar protons interacting with the SNR. Using the equations (1) and (2), the averaged number density of interstellar protons in molecular form is estimated to be $\sim 650 \pm 200 \text{ cm}^{-3}$ assuming a shell radius of 8 pc and a thickness of 3 pc (e.g., Moffett & Reynolds 1994). The error is derived as the typical uncertainty of the CO-to- H_2 conversion factor of $\sim 30\%$ (cf. Bolatto et al. 2013). Additionally, the interstellar protons in atomic form are neglectable in W49B because the derived column density of atomic hydrogen is significantly lower than that of molecular hydrogen (see Brogan & Troland 2001). The similar situation is also seen in other middle-aged SNRs (e.g., W44, Yoshiike et al. 2013). We

therefore adopt the number density of interstellar protons n_p to be $\sim 650 \pm 200 \text{ cm}^{-3}$.

According to [H. E. S. S. Collaboration et al. \(2018\)](#), the total energy of CR protons W_p is written as

$$W_p \sim 2.0\text{--}2.2 \times 10^{49} (n_p/650 \text{ cm}^{-3})^{-1} (d/11 \text{ kpc})^{-2} \text{ erg}, \quad (3)$$

where d is the distance to the SNR. Adopting $n_p = 650 \text{ cm}^{-3}$ and $d = 11 \text{ kpc}$, we then obtain $W_p \sim 2 \times 10^{49} \text{ erg}$, corresponding to $\sim 2\%$ of the typical kinematic energy released by a supernova explosion. Table 2 compares physical properties of eleven gamma-ray SNRs including W49B. Here, all values of n_p and W_p were derived from CO/H I radio-line observations. We find that W_p in W49B is roughly consistent with that in other gamma-ray bright SNRs located in our Galaxy or the Large Magellanic Cloud (LMC). In addition, it is noteworthy that young SNRs RX J1713.7–3946, RX J0852.0–4622 (a.k.a. Vela Jr.), and RCW 86 as well as an evolved SNR IC 443 show the lowest values of $W_p \sim 10^{48} \text{ erg}$, while the others hold higher values of $W_p \sim 10^{49} \text{ erg}$.

To better understand the trend, we plot W_p values as a function of the age of SNRs. Figure 10 shows a scatter plot between the age of SNRs and W_p . We find a positive correlation between two parameters in the SNRs with a young age less than ~ 6000 yrs, suggesting that in-situ values of W_p are strongly limited by short duration time of acceleration also known as age-limited acceleration (cf. [Ohira et al. 2010](#)). On the other hand, other SNRs with an older age more than ~ 8000 yrs show a steady decrease of W_p as SNRs get older. This trend could be understood considering the energy dependent diffusion of CRs (e.g., [Aharonian & Atoyan 1996](#); [Gabici et al. 2007](#)). In other words, in-situ values of W_p have been decreased due to CR escape from the SNR. In fact, hadron-dominant gamma-rays have been detected in nearby giant molecular clouds of W44, suggesting that the molecular clouds are illuminated by CR protons escaped from W44 (e.g., [Uchiyama et al. 2012](#); [Peron et al. 2020](#)). The authors suggested an actual value of W_p including escaped CRs is $\sim 10^{50} \text{ erg}$, corresponding to 10% of the typical kinematic energy released by a supernova explosion. In any case, W49B shows one of the highest in-situ values of W_p in the gamma-ray bright SNRs, which imply that the escape (diffusion) of CRs is not significant at the moment. Further gamma-ray observations using the Cherenkov Telescope Array (CTA) will unveil a transition phase from the age-limited acceleration to escape dominant stage in detail.

5. CONCLUSIONS

We summarize the primary conclusions as follows:

1. New ALMA ACA CO($J = 2\text{--}1$) observations at $\sim 7''$ resolution have revealed the spatial and kinematic distributions of three candidates of interacting molecular clouds with the mixed-morphology SNR W49B, velocities of which are $\sim 10 \text{ km s}^{-1}$,

$\sim 40 \text{ km s}^{-1}$, and $\sim 60 \text{ km s}^{-1}$. We found that western molecular clouds at $\sim 10 \text{ km s}^{-1}$ are obviously along with both the radio continuum boundary and inside filaments as well as the deformed X-ray shell, suggesting that shock-cloud interactions occurred. The 10 km s^{-1} cloud also shows higher kinetic temperature of $\sim 20\text{--}60 \text{ K}$ than the reference clouds at 15 K , indicating that modest shock heating also occurred. The presence of a wind-bubble with an expanding velocity of $\sim 6 \text{ km s}^{-1}$ provides further evidence for the association of the 10 km s^{-1} cloud.

2. The barrel-like structure of Fe-rich ejecta is mainly located on the void of dense molecular clouds, where a cool plasma component is enhanced. We propose a possible scenario that the barrel-like structure of Fe-rich ejecta was formed not only by the asymmetric supernova explosion, but also by interactions with dense molecular clouds. A supernova explosion occurred within the cylinder-like gaseous medium and then Fe-rich ejecta was efficiently heated-up at higher densities by multiple-reflected shocks formed by shock-cloud interactions.
3. The electron temperature kT_e of recombining plasma from Fe He α shows a negative correlation with the peak integrated intensity of CO line emission in the 10 km s^{-1} cloud. More precisely, kT_e values in high-temperature recombining plasma are increasing from the west (cloud rich) regions to the east (cloud poor) regions, suggesting the thermal conduction origin. Note that this finding does not rule out the adiabatic cooling scenario in the low-temperature recombining plasma in W49B which was previously discussed ([Sun & Chen 2020](#); [Holland-Ashford et al. 2020](#)).
4. The total energy of CR protons W_p is estimated to be $\sim 2 \times 10^{49} \text{ erg}$, which is one of the highest values in gamma-ray bright SNRs. We found that in-situ values of W_p in gamma-ray SNRs increase with age for the young group (with the age less than ~ 6000 yr). On the other hand, other older SNRs show a steady decrease of W_p as SNRs get older due to the escapes/diffusion effect of CRs. We frame a hypothesis that W49B is undergoing an age-limited acceleration without a significant escape or diffusion of CRs from the SNR.

ACKNOWLEDGEMENTS

We are grateful Hiroya Yamaguchi for providing us with the *NuSTAR* data points used in this paper. This paper makes use of the following ALMA data: ADS/JAO.ALMA#2018.1.01780.S. ALMA is a partnership of ESO (representing its member states), NSF (USA) and NINS (Japan), together with NRC

(Canada), MOST and ASIAA (Taiwan), and KASI (Republic of Korea), in cooperation with the Republic of Chile. The Joint ALMA Observatory is operated by ESO, AUI/NRAO and NAOJ. The scientific results reported in this article are based on data obtained from the *Chandra* Data Archive (Obs IDs: 117, 13440, and 13441). This research has made use of software provided by the *Chandra* X-ray Center (CXC) in the application packages CIAO (v 4.12). This work was supported by JSPS KAKENHI Grant Numbers JP19H05075 (H. Sano), and JP21H01136 (H. Sano). K. Tokuda was sup-

ported by NAOJ ALMA Scientific Research Grant Number of 2016-03B. We are also grateful to the anonymous referee for useful comments which helped the authors to improve the paper significantly.

Software: CASA (v 5.6.0.: McMullin et al. 2007), CIAO (v 4.12: Fruscione et al. 2006), CALDB (v 4.9.1 Graessle et al. 2007).

Facilities: ALMA, Chandra, NuSTAR, Very Large Array (VLA), Nobeyama 45-m Telescope, James Clerk Maxwell Telescope (JCMT).

REFERENCES

- Abdo, A. A., Ackermann, M., Ajello, M., et al. 2010, *ApJ*, 722, 1303. doi:10.1088/0004-637X/722/2/1303
- Ackermann, M., Ajello, M., Allafort, A., et al. 2013, *Science*, 339, 807. doi:10.1126/science.1231160
- Aharonian, F. A., Drury, L. O., & Voelk, H. J. 1994, *A&A*, 285, 645
- Aharonian, F. A. & Atoyan, A. M. 1996, *A&A*, 309, 917
- Aharonian, F., Akhperjanian, A. G., Bazer-Bachi, A. R., et al. 2008, *A&A*, 481, 401. doi:10.1051/0004-6361/20077765
- Anderl, S., Gusdorf, A., & Güsten, R. 2014, *A&A*, 569, A81. doi:10.1051/0004-6361/201423561
- Bamba, A., Sawada, M., Nakano, Y., et al. 2016, *PASJ*, 68, S5. doi:10.1093/pasj/psv096
- Bamba, A., Ohira, Y., Yamazaki, R., et al. 2018, *ApJ*, 854, 71. doi:10.3847/1538-4357/aaa5a0
- Bear, E. & Soker, N. 2017, *MNRAS*, 468, 140. doi:10.1093/mnras/stx431
- Biegging, J. H. & Peters, W. L. 2011, *ApJS*, 196, 18. doi:10.1088/0067-0049/196/2/18
- Beichman, C. A., Neugebauer, G., Habing, H. J., et al. 1988, *Infrared astronomical satellite (IRAS) catalogs and atlases. Volume 1: Explanatory supplement*, 1
- Bell, A. R. 1978, *MNRAS*, 182, 147. doi:10.1093/mnras/182.2.147
- Bertsch, D. L., Dame, T. M., Fichtel, C. E., et al. 1993, *ApJ*, 416, 587. doi:10.1086/173261
- Blandford, R. D. & Ostriker, J. P. 1978, *ApJL*, 221, L29. doi:10.1086/182658
- Blake, G. A., Sutton, E. C., Masson, C. R., et al. 1987, *ApJ*, 315, 621. doi:10.1086/165165
- Bolatto, A. D., Wolfire, M., & Leroy, A. K. 2013, *ARA&A*, 51, 207. doi:10.1146/annurev-astro-082812-140944
- Brand, J. & Blitz, L. 1993, *A&A*, 275, 67
- Brogan, C. L. & Troland, T. H. 2001, *ApJ*, 550, 799. doi:10.1086/319787
- Caswell, J. L., Murray, J. D., Roger, R. S., et al. 1975, *A&A*, 45, 239
- Celli, S., Morlino, G., Gabici, S., et al. 2019, *MNRAS*, 487, 3199. doi:10.1093/mnras/stz1425
- Dell’Ova, P., Gusdorf, A., Gerin, M., et al. 2020, *A&A*, 644, A64. doi:10.1051/0004-6361/202038339
- Dempsey, J. T., Thomas, H. S., & Currie, M. J. 2013, *ApJS*, 209, 8. doi:10.1088/0067-0049/209/1/8
- de Oña Wilhelmi, E., Sushch, I., Brose, R., et al. 2020, *MNRAS*, 497, 3581. doi:10.1093/mnras/staa2045
- Drury, L. O., Aharonian, F. A., & Voelk, H. J. 1994, *A&A*, 287, 959
- Ergin, T., Sezer, A., Saha, L., et al. 2014, *ApJ*, 790, 65. doi:10.1088/0004-637X/790/1/65
- Ergin, T., Sezer, A., Sano, H., et al. 2017, *ApJ*, 842, 22. doi:10.3847/1538-4357/aa72ee
- Fukuda, T., Yoshiike, S., Sano, H., et al. 2014, *ApJ*, 788, 94. doi:10.1088/0004-637X/788/1/94
- Fukui, Y., Mizuno, N., Yamaguchi, R., et al. 1999, *PASJ*, 51, 745. doi:10.1093/pasj/51.6.745
- Fukui, Y., Moriguchi, Y., Tamura, K., et al. 2003, *PASJ*, 55, L61. doi:10.1093/pasj/55.5.L61
- Fukui, Y., Sano, H., Sato, J., et al. 2012, *ApJ*, 746, 82. doi:10.1088/0004-637X/746/1/82
- Fukui, Y., Sano, H., Sato, J., et al. 2017, *ApJ*, 850, 71. doi:10.3847/1538-4357/aa9219
- Fruscione, A., McDowell, J. C., Allen, G. E., et al. 2006, *Proc. SPIE*, 6270, 62701V. doi:10.1117/12.671760
- Gabici, S., Aharonian, F. A., & Blasi, P. 2007, *Ap&SS*, 309, 365. doi:10.1007/s10509-007-9427-6
- Gabici, S. 2013, *Cosmic Rays in Star-Forming Environments*, 34, 221. doi:10.1007/978-3-642-35410-6_16
- Giuliani, A., Cardillo, M., Tavani, M., et al. 2011, *ApJL*, 742, L30. doi:10.1088/2041-8205/742/2/L30
- Goldreich, P. & Kwan, J. 1974, *ApJ*, 189, 441. doi:10.1086/152821
- Graessle, D. E., Evans, I. N., Glotfelty, K., et al. 2007, *Chandra Newsletter*, Vol. 14, p.33, 14
- Gusdorf, A., Anderl, S., Güsten, R., et al. 2012, *A&A*, 542, L19. doi:10.1051/0004-6361/201218907

- H. E. S. S. Collaboration, Abdalla, H., Abramowski, A., et al. 2018, *A&A*, 612, A5.
doi:10.1051/0004-6361/201527843
- Helfand, D. J., Becker, R. H., White, R. L., et al. 2006, *AJ*, 131, 2525. doi:10.1086/503253
- Hirayama, A., Yamauchi, S., Nobukawa, K. K., et al. 2019, *PASJ*, 71, 37. doi:10.1093/pasj/psy153
- Holland-Ashford, T., Lopez, L. A., & Auchettl, K. 2020, *ApJ*, 903, 108. doi:10.3847/1538-4357/abb808
- Hughes, J. P., Hayashi, I., & Koyama, K. 1998, *ApJ*, 505, 732. doi:10.1086/306202
- Inoue, T., Yamazaki, R., & Inutsuka, S.-. ichiro . 2009, *ApJ*, 695, 825. doi:10.1088/0004-637X/695/2/825
- Inoue, T., Yamazaki, R., Inutsuka, S.-. ichiro ., et al. 2012, *ApJ*, 744, 71. doi:10.1088/0004-637X/744/1/71
- Itoh, H. & Masai, K. 1989, *MNRAS*, 236, 885.
doi:10.1093/mnras/236.4.885
- Kamitsukasa, F., Koyama, K., Uchida, H., et al. 2015, *PASJ*, 67, 16. doi:10.1093/pasj/psu149
- Katsuragawa, M., Nakashima, S., Matsumura, H., et al. 2018, *PASJ*, 70, 110. doi:10.1093/pasj/psy114
- Kawasaki, M. T., Ozaki, M., Nagase, F., et al. 2002, *ApJ*, 572, 897. doi:10.1086/340383
- Kawasaki, M., Ozaki, M., Nagase, F., et al. 2005, *ApJ*, 631, 935. doi:10.1086/432591
- Kepley, A. A., Tsutsumi, T., Brogan, C. L., et al. 2020, *PASP*, 132, 024505. doi:10.1088/1538-3873/ab5e14
- Katsuda, S., Tsunemi, H., & Mori, K. 2008, *ApJL*, 678, L35. doi:10.1086/588499
- Kawamura, A., Mizuno, Y., Minamidani, T., et al. 2009, *ApJS*, 184, 1. doi:10.1088/0067-0049/184/1/1
- Keohane, J. W., Reach, W. T., Rho, J., et al. 2007, *ApJ*, 654, 938. doi:10.1086/509311
- Kerr, F. J. & Lynden-Bell, D. 1986, *MNRAS*, 221, 1023.
doi:10.1093/mnras/221.4.1023
- Kilpatrick, C. D., Biegging, J. H., & Rieke, G. H. 2016, *ApJ*, 816, 1. doi:10.3847/0004-637X/816/1/1
- Koo, B.-C., Reach, W. T., Heiles, C., et al. 1990, *ApJ*, 364, 178. doi:10.1086/169400
- Koo, B.-C. & Heiles, C. 1991, *ApJ*, 382, 204.
doi:10.1086/170709
- Koo, B.-C., Lee, J.-J., Jeong, I.-G., et al. 2016, *ApJ*, 821, 20. doi:10.3847/0004-637X/821/1/20
- Kuriki, M., Sano, H., Kuno, N., et al. 2018, *ApJ*, 864, 161.
doi:10.3847/1538-4357/aad7be
- Langer, W. D. & Penzias, A. A. 1990, *ApJ*, 357, 477.
doi:10.1086/168935
- Law, C. J., Milisavljevic, D., Patnaude, D. J., et al. 2020, *ApJ*, 894, 73. doi:10.3847/1538-4357/ab873a
- Leahy, D., Wang, Y., Lawton, B., et al. 2019, *AJ*, 158, 149.
doi:10.3847/1538-3881/ab3d2c
- Lee, J.-J., Koo, B.-C., Yun, M. S., et al. 2008, *AJ*, 135, 796.
doi:10.1088/0004-6256/135/3/796
- Lee, Y.-H., Koo, B.-C., & Lee, J.-J. 2020, *AJ*, 160, 263.
doi:10.3847/1538-3881/abc00e
- Liu, B., Anderson, L. D., McIntyre, T., et al. 2019, *ApJS*, 240, 14. doi:10.3847/1538-4365/aaef8e
- Lockhart, I. A. & Goss, W. M. 1978, *A&A*, 67, 355
- Lopez, L. A., Ramirez-Ruiz, E., Pooley, D. A., et al. 2009a, *ApJ*, 691, 875. doi:10.1088/0004-637X/691/1/875
- Lopez, L. A., Ramirez-Ruiz, E., Badenes, C., et al. 2009b, *ApJL*, 706, L106. doi:10.1088/0004-637X/706/1/L106
- Lopez, L. A., Ramirez-Ruiz, E., Huppenkothen, D., et al. 2011, *ApJ*, 732, 114. doi:10.1088/0004-637X/732/2/114
- Lopez, L. A., Pearson, S., Ramirez-Ruiz, E., et al. 2013a, *ApJ*, 777, 145. doi:10.1088/0004-637X/777/2/145
- Lopez, L. A., Ramirez-Ruiz, E., Castro, D., et al. 2013b, *ApJ*, 764, 50. doi:10.1088/0004-637X/764/1/50
- Masai, K. 1994, *ApJ*, 437, 770. doi:10.1086/175037
- Matsumura, H., Uchida, H., Tanaka, T., et al. 2017a, *PASJ*, 69, 30. doi:10.1093/pasj/psx001
- Matsumura, H., Tanaka, T., Uchida, H., et al. 2017b, *ApJ*, 851, 73. doi:10.3847/1538-4357/aa9bdf
- McMullin, J. P., Waters, B., Schiebel, D., et al. 2007, *Astronomical Data Analysis Software and Systems XVI*, 376, 127
- Miceli, M., Bocchino, F., Decourchelle, A., et al. 2010, *A&A*, 514, L2. doi:10.1051/0004-6361/200913713
- Moffett, D. A. & Reynolds, S. P. 1994, *ApJ*, 437, 705.
doi:10.1086/175033
- Mouri, H. 1994, *ApJ*, 427, 777. doi:10.1086/174184
- Nakashima, S., Nobukawa, M., Uchida, H., et al. 2013, *ApJ*, 773, 20. doi:10.1088/0004-637X/773/1/20
- Ohira, Y., Murase, K., & Yamazaki, R. 2010, *A&A*, 513, A17. doi:10.1051/0004-6361/200913495
- Ohnishi, T., Koyama, K., Tsuru, T. G., et al. 2011, *PASJ*, 63, 527. doi:10.1093/pasj/63.3.527
- Okon, H., Uchida, H., Tanaka, T., et al. 2018, *PASJ*, 70, 35.
doi:10.1093/pasj/psy022
- Okon, H., Tanaka, T., Uchida, H., et al. 2020, *ApJ*, 890, 62.
doi:10.3847/1538-4357/ab6987
- Olbert, C. M., Clearfield, C. R., Williams, N. E., et al. 2001, *ApJL*, 554, L205. doi:10.1086/321708
- Ono, A., Uchiyama, H., Yamauchi, S., et al. 2019, *PASJ*, 71, 52. doi:10.1093/pasj/psz025
- Ozawa, M., Koyama, K., Yamaguchi, H., et al. 2009, *ApJL*, 706, L71. doi:10.1088/0004-637X/706/1/L71
- Peron, G., Aharonian, F., Casanova, S., et al. 2020, *ApJL*, 896, L23. doi:10.3847/2041-8213/ab93d1

- Ranasinghe, S. & Leahy, D. A. 2018, *AJ*, 155, 204.
doi:10.3847/1538-3881/aab9be
- Rho, J. & Petre, R. 1998, *ApJL*, 503, L167.
doi:10.1086/311538
- Sano, H., Tanaka, T., Torii, K., et al. 2013, *ApJ*, 778, 59.
doi:10.1088/0004-637X/778/1/59
- Sano, H., Yamane, Y., Voisin, F., et al. 2017a, *ApJ*, 843, 61. doi:10.3847/1538-4357/aa73e0
- Sano, H., Reynoso, E. M., Mitsuishi, I., et al. 2017b, *Journal of High Energy Astrophysics*, 15, 1.
doi:10.1016/j.jheap.2017.04.002
- Sano, H., Rowell, G., Reynoso, E. M., et al. 2019a, *ApJ*, 876, 37. doi:10.3847/1538-4357/ab108f
- Sano, H., Matsumura, H., Nagaya, T., et al. 2019b, *ApJ*, 873, 40. doi:10.3847/1538-4357/ab02fd
- Sano, H., Matsumura, H., Yamane, Y., et al. 2019c, *ApJ*, 881, 85. doi:10.3847/1538-4357/ab2ade
- Sano, H., Plucinsky, P. P., Bamba, A., et al. 2020a, *ApJ*, 902, 53. doi:10.3847/1538-4357/abb469
- Sano, H., Inoue, T., Tokuda, K., et al. 2020b, *ApJL*, 904, L24. doi:10.3847/2041-8213/abc884
- Sano, H. & Fukui, Y. 2021, arXiv:2106.00708
- Sawada, M. & Koyama, K. 2012, *PASJ*, 64, 81.
doi:10.1093/pasj/64.4.81
- Scoville, N. Z. & Solomon, P. M. 1974, *ApJL*, 187, L67.
doi:10.1086/181398
- Seta, M., Hasegawa, T., Dame, T. M., et al. 1998, *ApJ*, 505, 286. doi:10.1086/306141
- Siegel, J., Dwarkadas, V. V., Frank, K. A., et al. 2020, *ApJ*, 904, 175. doi:10.3847/1538-4357/abffa9
- Shimizu, T., Masai, K., & Koyama, K. 2012, *PASJ*, 64, 24.
doi:10.1093/pasj/64.2.24
- Slavin, J. D., Smith, R. K., Foster, A., et al. 2017, *ApJ*, 846, 77. doi:10.3847/1538-4357/aa8552
- Sofue, Y., Kohno, M., & Umemoto, T. 2020, arXiv:2011.11916
- Sofue, Y. 2020, *PASJ*, 72, L11. doi:10.1093/pasj/psaa102
- Su, Y., Chen, Y., Yang, J., et al. 2011, *ApJ*, 727, 43.
doi:10.1088/0004-637X/727/1/43
- Sun, L. & Chen, Y. 2020, *ApJ*, 893, 90.
doi:10.3847/1538-4357/ab8001
- Suzuki, H., Bamba, A., Nakazawa, K., et al. 2018, *PASJ*, 70, 75. doi:10.1093/pasj/psy069
- Tanaka, T., Yamaguchi, H., Wik, D. R., et al. 2018, *ApJL*, 866, L26. doi:10.3847/2041-8213/aae709
- Uchida, H., Koyama, K., Yamaguchi, H., et al. 2012, *PASJ*, 64, 141. doi:10.1093/pasj/64.6.141
- Uchida, H., Koyama, K., & Yamaguchi, H. 2015, *ApJ*, 808, 77. doi:10.1088/0004-637X/808/1/77
- Uchiyama, Y., Funk, S., Katagiri, H., et al. 2012, *ApJL*, 749, L35. doi:10.1088/2041-8205/749/2/L35
- Umemoto, T., Minamidani, T., Kuno, N., et al. 2017, *PASJ*, 69, 78. doi:10.1093/pasj/psx061
- Urquhart, J. S., Hoare, M. G., Purcell, C. R., et al. 2009, *A&A*, 501, 539. doi:10.1051/0004-6361/200912108
- VERA Collaboration, Hirota, T., Nagayama, T., et al. 2020, *PASJ*, 72, 50. doi:10.1093/pasj/psaa018
- Vink, J. 2012, *A&A Rv*, 20, 49.
doi:10.1007/s00159-011-0049-1
- Washino, R., Uchida, H., Nobukawa, M., et al. 2016, *PASJ*, 68, S4. doi:10.1093/pasj/psv095
- Welsh, B. Y. & Sallmen, S. 2003, *A&A*, 408, 545.
doi:10.1051/0004-6361:20030908
- Wolszczan, A., Cordes, J. M., & Dewey, R. J. 1991, *ApJL*, 372, L99. doi:10.1086/186033
- XRISM Science Team 2020, arXiv:2003.04962
- Yamaguchi, H., Badenes, C., Petre, R., et al. 2014, *ApJL*, 785, L27. doi:10.1088/2041-8205/785/2/L27
- Yamaguchi, H., Tanaka, T., Wik, D. R., et al. 2018, *ApJL*, 868, L35. doi:10.3847/2041-8213/aaf055
- Yamaguchi, H. 2020, *Astronomische Nachrichten*, 341, 150.
doi:10.1002/asna.202023771
- Yamauchi, S., Minami, S., Ota, N., et al. 2014, *PASJ*, 66, 2.
doi:10.1093/pasj/pst004
- Yamane, Y., Sano, H., van Loon, J. T., et al. 2018, *ApJ*, 863, 55. doi:10.3847/1538-4357/aacfff
- Yamauchi, S., Oya, M., Nobukawa, K. K., et al. 2020, *PASJ*, 72, 81. doi:10.1093/pasj/psaa070
- Yamauchi, S., Nobukawa, M., Koyama, K., et al. 2013, *PASJ*, 65, 6. doi:10.1093/pasj/65.1.6
- Yang, X. J., Tsunemi, H., Lu, F. J., et al. 2009, *ApJ*, 692, 894. doi:10.1088/0004-637X/692/1/894
- Yoshiike, S., Fukuda, T., Sano, H., et al. 2013, *ApJ*, 768, 179. doi:10.1088/0004-637X/768/2/179
- Yoshiike, S., Sano, H., Fukuda, T., et al. 2021, to be submitted
- Yusef-Zadeh, F., Wardle, M., Rho, J., et al. 2003, *ApJ*, 585, 319. doi:10.1086/345932
- Zhang, G.-Y., Slavin, J. D., Foster, A., et al. 2019, *ApJ*, 875, 81. doi:10.3847/1538-4357/ab0f9a
- Zhou, X., Miceli, M., Bocchino, F., et al. 2011, *MNRAS*, 415, 244. doi:10.1111/j.1365-2966.2011.18695.x
- Zhou, P. & Vink, J. 2018, *A&A*, 615, A150.
doi:10.1051/0004-6361/201731583
- Zhu, H., Tian, W. W., & Zuo, P. 2014, *ApJ*, 793, 95.
doi:10.1088/0004-637X/793/2/95